Article

MMS

Mathematics and Mechanics of Solids
2020, Vol. 25(3) 739–767

DOI: 10.1177/1081286519891228
journals.sagepub.com/home/mms
SAGE

Large in-plane elastic deformations of bi-pantographic fabrics: asymptotic homogenization and experimental validation

Emilio Barchiesi
Dipartimento di Ingegneria Strutturale e Geotecnica, Università degli Studi di Roma "La Sapienza", Italy International Research Center M&MoCS, Università degli Studi dell'Aquila, Italy

Simon R Eugster
Institute for Nonlinear Mechanics, University of Stuttgart, Germany

Francesco dell'Isola
Dipartimento di Ingegneria Civile, Edile-Architettura e Ambientale, Università degli Studi dell'Aquila, Italy Dipartimento di Ingegneria Strutturale e Geotecnica, Università degli Studi di Roma "La Sapienza", Italy International Research Center M&MoCS, Università degli Studi dell'Aquila, Italy

François Hild
Laboratoire de Mécanique et Technologie (LMT) ENS Paris-Saclay/CNRS/Univ. Paris-Saclay, France

Received 10 October 2019; accepted 27 October 2019

Abstract
Bi-pantographic fabrics are composed of two families of pantographic beams and correspond to a class of architectured materials that are described in plane as second-gradient 2D continua. On a discrete level, a pantographic beam is a periodic arrangement of cells and looks like an expanding barrier. The materialization of a bi-pantographic fabric made from polyamide was achieved by additive manufacturing techniques. Starting from a discrete spring system, the deformation energy of the corresponding continuum is derived for large strains by asymptotic homogenization. The obtained energy depends on the second gradient of the deformation through the rate of change in orientation and stretch of material lines directed along the pantographic beams. Displacement-controlled bias extension tests were performed on rectangular prototypes for total elastic extension up to 25%. Force–displacement measurements complemented by local digital image correlation analyses were used to fit the continuum model achieving excellent agreement.

Corresponding author:
Emilio Barchiesi, Dipartimento di Ingegneria Strutturale e Geotecnica, Università degli Studi di Roma "La Sapienza", Via Eudossiana 18, Rome 00184, Italy.
Email: barchiesiemilio@gmail.com

Keywords
variational asymptotic homogenization, bi-pantographic fabrics, second gradient continua, additive manufacturing, local digital image correlation, Piola's ansatz, experimental mechanics

1. Introduction

Continuum modelling, i.e., spatially continuous formulations [1-5], is routinely exploited to describe at macro length scales the collective behaviour of (mostly periodic) discrete systems, whose element-by-element micro-scale description [6-10] can be computationally challenging. Homogenization procedures [11–15] can be used to pass from a discrete to a continuous description. These procedures involve the definition of specific micro–macro correspondences [16], which enable precise meanings to be given to many features of the macro-model in terms of those of the micro-model.

The last few decades have witnessed a high acceleration in the development of additive and subtractive techniques such as 3D printing [17]. Such techniques allow for micro-structure control at very small scales, which motivate the renewed interest in homogenization [18–22].

Pantographic structures [23–25] are among the most straightforward examples of micro-structures whose continuum modelling gives a wealth of non-standard problems in the theory of higher-gradient [26-28] and micromorphic continua [11, 29-31], also of mathematical interest [32]. Convenient discrete descriptions of pantographic structures have been obtained in the literature by Hencky-type modelling [7, 8, 30].

The derivation of a 1D continuum model being capable of describing the finite planar deformation of a discrete slender pantographic structure, referred to as pantographic beam, was presented in [33]. The continuum model is deduced from a discrete one by applying a variational asymptotic procedure [11, 20, 34, 35]. Within the homogenization process, the overall dimension of the system is kept fixed, while the number of the periodically appearing subsystems, called cells, is increased, and the stiffnesses are scaled appropriately.

In [33], the model of [34, 35] has been generalized to the finite strain regime. Remarkably, the deformation energy density of such a 1D continuum [33] does not only depend on the material curvature but also on the stretch gradient. In addition to a more pedagogical presentation of such a continuum model, Barchiesi et al. [36] addressed numerically the evaluation of differences between the micro- and the macro-model in order to elucidate to what extent the continuum retains the relevant phenomenology of the discrete system. Special attention has been given to the difference between the deformation energy of the micro- and the macro-model when the micro length scale tends to zero, i.e. the discrete-continuum error. This deviation gives a quantitative value to assess the quality of the approximation of the discrete by its continuous counterpart.

Bi-pantographic fabrics were first introduced by Seppecher et al. [35] as assemblies of discrete pantographic beams leading at macroscopic scale to second gradient materials [37-39]. The corresponding deformation energy depends upon the rate of change in orientation and stretch of material lines directed along the pantographic beams. The aims of this work are as followings. First, we want to generalize the homogenization carried out in [35] in two respects. In particular, extensible elements and arbitrarily large strains are considered. Second, a possible design of bi-pantographic prototypes is sought, which is obeying the discrete model. Lastly, the derived results will be validated.

Addressing the above objectives leads to the following organization of the article. In Section 2, the discrete bi-pantographic structure is introduced followed by a homogenization that is carried out by exploiting the results obtained for pantographic beams. In Section 3, we establish relations between quantities for the microscopic and macroscopic models, which go beyond Piola's micro–macro identification used throughout the homogenization. Based on these relations, a non-standard bias extension test is then introduced for both models. Lastly, the finite element method employed to solve the continuum model is introduced with a special emphasis on the challenges arising from a weak mixed formulation. In Section 4, the design and manufacturing of a bi-pantographic prototype is reported together with the description of the experimental setup. The digital image correlation (DIC) technique used to retrieve discrete displacement measures is also briefly recalled. In Section 5, the fitting of parameters by means of acquired experimental measures is presented and continuum is compared with experiments.

2. Heuristic homogenization

The continuum is deduced by applying Piola's micro–macro identification procedure [11, 40], which can be considered as a heuristic variational asymptotic procedure. The steps describing such a procedure can be sketched as follows.

(i) A family of discrete spring systems embedded in the 2D Euclidean vector space $\mathbb{E}^2$, i.e. the micro-model with micro length scale $\varepsilon > 0$, is introduced: generalized coordinates and energy contributions $\mathfrak{E}_\varepsilon$ are defined.
(ii) The kinematic descriptors of the continuum, i.e. the macro-model, are introduced as continuous functions with a closed subset of $\mathbb{E}^2$ as their common domain: these functions must be chosen such that their evaluation at particular points can be related to the generalized coordinates of the micro-model.
(iii) Formulation of the deformation energy of the micro-model $\mathfrak{E}_\varepsilon$ using the evaluation of the continuum descriptors at particular points, followed by a Taylor expansion of the energy with respect to the micro length scale ε.
(iv) Specification of scaling laws for the constitutive parameters in the micro-model followed by a limit process in which the energy of the continuum $\mathfrak{E}$ is related to the micro-model by $\mathfrak{E} = \lim_{\varepsilon\to 0} \mathfrak{E}_\varepsilon$

2.1. Preliminaries

To ease the presentation, before addressing bi-pantographic structures, some preliminary computations related to pantographic beams are revisited.

2.1.1. Pantographic beam: discrete model. The assembly and kinematics of a discrete pantographic beam slightly generalizing that presented in [33, 36] are sketched in Figure 1. In the undeformed configuration, see Figure 1(a), N cells are arranged upon a straight line along the direction of the unit basis vector $e_x \in \mathbb{E}^2$. The total length $L \in \mathbb{R}$ of the undeformed pantographic beam accounts for $N-1$ cells, as depicted in

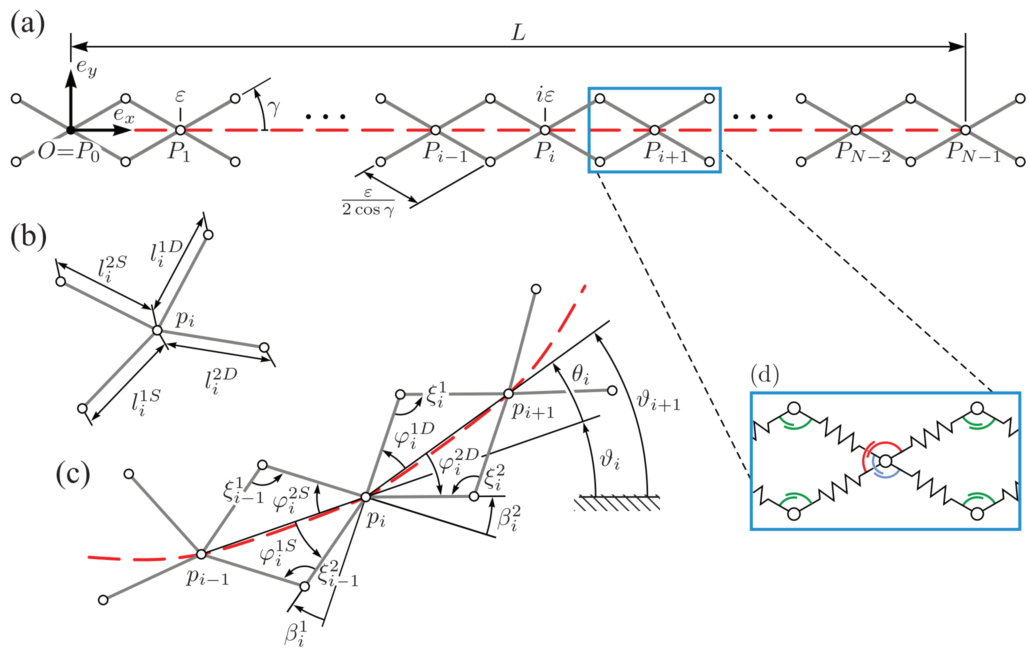

Figure 1. Pantographic beam. (a) Undeformed configuration. (b) Generalized coordinates of the *i*th cell. (c) Deformed configuration with redundant kinematic quantities. (d) Force elements of a single cell.

Figure 1(a). The cells are centred at the positions $P_i = i\varepsilon e_x$ for $i \in \{0, 1, \ldots, N-1\}$ with $\varepsilon = L/(N-1)$. The basic ith unit cell is formed by four extensional springs hinge-joined together at P_i having length $\varepsilon/(2\cos\gamma)$. Rotational springs, which are coloured in blue, red and green in Figure 1(d), are placed between opposite collinear and adjacent springs belonging to the same cell and between adjacent springs belonging to different cells. Note that extensional springs are rigid with respect to bending such that they can transmit torques. White-filled circles in Figure 1 depict hinge constraints, requiring the end points of the corresponding springs to have the same position in space. We note that the assembly considered herein is a generalization of that studied in [33], as the angle $\gamma \in (0, \pi)$ between springs concurring at point P_i from the right in Figure [33] is generally different from $\pi/4$. Moreover, further rotational springs, which are coloured in green in Figure 1(d), are considered. When not otherwise mentioned, the indices i, μ and ν henceforth belong to the sets $i \in \{0, 1, \ldots, N-1\}$, $\mu \in \{1, 2\}$ and $\nu \in \{D, S\}$, respectively.[1]

The kinematics of the spring system is locally described by finitely many generalized coordinates. The coordinates are the positions $p_i \in \mathbb{E}^2$ of the points at position P_i in the reference configuration and the lengths of the oblique deformed springs $l_i^{\mu\nu} \in \mathbb{R}$. Various other kinematical quantities are considered to formulate the total potential energy in a most compact form. Applying the law of cosines, the angles $\varphi_i^{\mu\nu}$ depicted in Figure 1(c) are determined by the following relationships

$$
\begin{aligned}
\varphi_i^{1D} &= \cos^{-1}\left[\frac{\| p_{i+1} - p_i\|^2 + (l_i^{1D})^2 - (l_{i+1}^{2S})^2}{2 l_i^{1D} \| p_{i+1} - p_i \|}\right],\\
\varphi_i^{1S} &= \cos^{-1}\left[\frac{\| p_i - p_{i-1}\|^2 + (l_i^{1S})^2 - (l_{i-1}^{2D})^2}{2 l_i^{1S} \| p_i - p_{i-1} \|}\right],\\
\varphi_i^{2D} &= \cos^{-1}\left[\frac{\| p_{i+1} - p_i\|^2 + (l_i^{2D})^2 - (l_{i+1}^{1S})^2}{2 l_i^{2D} \| p_{i+1} - p_i \|}\right],\\
\varphi_i^{2S} &= \cos^{-1}\left[\frac{\| p_i - p_{i-1}\|^2 + (l_i^{2S})^2 - (l_{i-1}^{1D})^2}{2 l_i^{2S} \| p_i - p_{i-1} \|}\right],
\end{aligned}
\tag{1}
$$

while the angles ξ_i^{μ} depicted in Figure 1(c) are determined by

$$
\xi_i^{1(2)} = \cos^{-1}\left[\frac{(l_i^{1(2)D})^2 + (l_{i+1}^{2(1)S})^2 - \|p_{i+1} - p_i\|^2}{2 l_i^{1(2)D} l_{i+1}^{2(1)S}}\right]. \tag{2}
$$

For $a \in \mathbb{E}^2$, $\| a \| = \sqrt{a \cdot a}$ corresponds to the norm induced by the inner product denoted by the dot.

Note that $\varphi_0^{\mu S}$ and $\varphi_{N-1}^{\mu D}$ cannot be determined by Equations (1) and belong also to the set of generalized coordinates. Another restriction is that the choice of generalized coordinates holds only locally, as long as the angles φ_i^{1D} and φ_i^{2D} do not change sign. Throughout the derivation of the macro-model, it is assumed that the angles φ_i^{1D} and φ_i^{2D} remain in the range $(0, \pi)$. This entails that $\xi_i^{\mu} \in (0, \pi)$. For the reduced index set $i = \{1, 2, \ldots, N-2\}$, the angle between the two vectors $p_i - p_{i-1}$ and e_x is denoted by ϑ_i. Then the angle θ_i between the vectors $p_i - p_{i-1}$ and $p_{i+1} - p_i$ reads

$$
\theta_i = \vartheta_{i+1} - \vartheta_i = \tan^{-1}\left[\frac{(p_{i+1} - p_i) \cdot e_y}{(p_{i+1} - p_i) \cdot e_x}\right] - \tan^{-1}\left[\frac{(p_i - p_{i-1}) \cdot e_y}{(p_i - p_{i-1}) \cdot e_x}\right] \tag{3}
$$

Let us set $\theta_0 = \theta_1$ and $\theta_{N-1} = \theta_{N-2}$ such that the deviation angles of two adjacent oblique springs from being collinear are given for the entire index set of i by

$$
\beta_i^1 = \theta_i + \varphi_i^{1D} - \varphi_i^{1S}, \quad \beta_i^2 = \theta_i + \varphi_i^{2S} - \varphi_i^{2D}. \tag{4}
$$

For the undeformed configuration, see Figure 1(a), the following equalities are satisfied

$$
l_i^{\mu\nu} = \frac{1}{2\cos\gamma}\varepsilon, \quad \beta_i^1 = \beta_i^2 = 0, \quad \| p_i - p_{i-1} \| = \varepsilon. \tag{5}
$$

Letting the summations for i, μ and ν range over the above introduced sets $\{0, \ldots, N-1\}$, $\{1,2\}$ and $\{D,S\}$, respectively, the micro-model deformation energy is defined as

$$\begin{aligned}\mathcal{E}_\varepsilon = & \frac{k_E}{2}\sum_i\sum_{\mu,\nu}\left(l_i^{\mu\nu}-\frac{1}{2\cos\gamma}\varepsilon\right)^2+\frac{k_F}{2}\sum_i\sum_\mu(\beta_i^\mu)^2+\frac{k_S}{2}\sum_i\sum_\mu(\xi_i^\mu-\pi+2\gamma)^2 \\ \overset{(4)}{=} & \frac{k_E}{2}\sum_i\sum_{\mu,\nu}\left(l_i^{\mu\nu}-\frac{1}{2\cos\gamma}\varepsilon\right)^2+\frac{k_F}{2}\sum_i\sum_\mu\left[\theta_i+(-1)^\mu\left(\varphi_i^{\mu S}-\varphi_i^{\mu D}\right)\right]^2+\frac{k_S}{2}\sum_{i=0}^{N-2}\sum_\mu(\xi_i^\mu-\pi+2\gamma)^2,\end{aligned} \tag{6}$$

where $k_E > 0$ and $k_F, k_S > 0$ are the stiffnesses of the extensional and rotational springs, respectively. Boundedness of the deformation energy, both for the micro-model and for the macro-model is considered throughout this article. It is worth noting that, in addition to the rigid body modes, the set of admissible configurations defined by

$$l_i^{\mu\nu}=\frac{1}{2\cos\gamma}\varepsilon,\quad p_i=p_{i-1}+Ke_x,\quad p_0=P_0,\quad \text{for } K\in(0,\frac{1}{\cos\gamma}\varepsilon), \tag{7}$$

also entails null deformation energy when $k_S = 0$, i.e. when removing green springs in Figure 1(d), and is referred to as extensional floppy mode [34]. Looking at the points p_i, one observes uniform extension or compression.

For the lengths $l_i^{\mu\nu}$ of the oblique springs, the following asymptotic expansion is assumed

$$l_i^{\mu\nu}=\frac{1}{2\cos\gamma}\varepsilon+\varepsilon^2\tilde{l}_i^{\mu\nu}+o(\varepsilon^2), \tag{8}$$

where $\tilde{l}_i^{\mu\nu}\in\mathbb{R}$. Inserting assumption (8) into the energy (6) leads to

$$\mathcal{E}_\varepsilon=\tfrac{k_E}{2}\sum_i\sum_{\mu,\nu}\left[\varepsilon^2\tilde{l}_i^{\mu\nu}+o(\varepsilon^2)\right]^2+\tfrac{k_F}{2}\sum_i\sum_\mu\left[\theta_i+(-1)^\mu(\varphi_i^{\mu S}-\varphi_i^{\mu D})\right]^2+\tfrac{k_S}{2}\sum_i\sum_\mu(\xi_i^\mu-\pi+2\gamma)^2. \tag{9}$$

2.1.2. Pantographic beam: micro–macro identification. The slenderness of the discrete system makes it reasonable to aim for a one-dimensional continuum [41] in the limit of vanishing ε. The continuum is then parametrized by the arclength $s\in[0,L]$ of the straight segment of length L connecting all points P_i.

The independent kinematic Lagrangian descriptors of the macro-model are assumed to be the functions $\chi:\ [0,L]\to\mathbb{E}^2$ and $\tilde{l}^{\mu\nu}:[0,L]\to\mathbb{R}$. The placement function χ places the 1D continuum into $\mathbb{E}^2$ and is best suited to describe the points $p_i\in\mathbb{E}^2$ of the discrete system on a macro-level. To take into account also the effect of changing spring lengths $\tilde{l}_i^{\mu\nu}$ introduced in Equation (8), the placement function is augmented by the four micro-strain functions $\tilde{l}^{\mu\nu}$. The identification of the discrete system is possible with a one-dimensional continuum that is classified as a micromorphic continuum [42-45]. It is also convenient to introduce the functions $\rho:[0,L]\to\mathbb{R}^+$ and $\vartheta:[0,L]\to[0,2\pi)$ in order to rewrite the tangent vector field χ' to the deformed 1D continuum as

$$\chi'(s)=\rho(s)\left[\cos\vartheta(s)e_x+\sin\vartheta(s)e_y\right], \tag{10}$$

where prime denotes differentiation with respect to the reference arc length s. Thus ρ corresponds to the norm of the tangent vector $\|\chi'\|$ and is referred to as stretch. The current curve $\chi([0,L])$ can, in general, have a length $\int_0^L\rho\,\mathrm{d}s$ different from L, as s is not an arc-length parametrization for χ but for the reference placement $\chi_0(s)=se_x$. Introducing the normal vector field $\chi'_\perp(s)=\rho(s)\left[-\sin\vartheta(s)e_x+\cos\vartheta(s)e_y\right]$, being rotated against $\chi'(s)$ about 90° in the anti-clockwise direction, the following results are found

$$\rho'(s)=\frac{\chi'(s)\cdot\chi''(s)}{\|\chi'(s)\|},\quad \vartheta'(s)=\frac{\chi''(s)\cdot\chi'_\perp(s)}{\|\chi'(s)\|^2}. \tag{11}$$

In the following, ρ' and ϑ' are called the stretch gradient and material curvature, respectively. For Piola's micro–macro identification, the generalized coordinates of the discrete system are related to the functions χ and $\tilde{l}^{\mu\nu}$ evaluated at $s_i = i\varepsilon$ as

$$\chi(s_i) = p_i, \quad \tilde{l}^{\mu\nu}(s_i) = \tilde{l}_i^{\mu\nu}. \tag{12}$$

For the asymptotic identification, the energy (9) is expanded in ε. The expansion of χ is given by

$$\chi(s_{i\pm1}) = \chi(s_i) \pm \varepsilon\chi'(s_i) + \frac{\varepsilon^2}{2}\chi''(s_i) + o(\varepsilon^2). \tag{13}$$

Combining the asymptotic expansion (8) with $(12)_2$ and the expansion $\tilde{l}^{\mu\nu}(s_{i\pm1}) = \tilde{l}^{\mu\nu}(s_i) + o(\varepsilon^0)$, leads to

$$l_{i\pm1}^{\mu\nu} = \frac{1}{2\cos\gamma}\varepsilon + \tilde{l}^{\mu\nu}(s_i)\varepsilon^2 + o(\varepsilon^2). \tag{14}$$

In order to further expand (9), the terms θ_i, $\varphi_i^{\mu S} - \varphi_i^{\mu D}$ and ξ_i^μ are expanded up to first order (see Appendix A). For θ_i according to Equation (71)

$$\theta_i = \vartheta'(s_i)\varepsilon + o(\varepsilon). \tag{15}$$

The differences $\varphi_i^{1(2)S} - \varphi_i^{1(2)D}$ are given by Equation (78) as

$$\varphi_i^{1(2)S} - \varphi_i^{1(2)D} = \left.\frac{4[\rho^2 - (1/2\cos^2\gamma)](\tilde{l}^{1(2)S} - \tilde{l}^{1(2)D}) + (1/\cos\gamma)(\rho^2)' + (2/\cos^2\gamma)(\tilde{l}^{2(1)D} - \tilde{l}^{2(1)S})}{4\rho(1/2\cos\gamma)\sqrt{(1/\cos^2\gamma) - \rho^2}}\right|_{s=s_i}\varepsilon + o(\varepsilon). \tag{16}$$

The angles ξ_i^μ are given by (80) as

$$\xi_i^\mu = \cos^{-1}\left.\left(1 - \frac{\rho^2}{1/2\cos^2\gamma}\right)\right|_{s=s_i} + o(\varepsilon^0). \tag{17}$$

Substituting (15), (16) and (17) into (9) together with $\rho(s_i) = \parallel \chi'(s_i) \parallel$, the sought expansion of the micro-model energy $\mathcal{E}_\varepsilon$ as a function of the kinematic descriptors χ and $l^{\mu\nu}$ reads

$$\begin{aligned}\mathcal{E}_\varepsilon = &\sum_i \left\{\frac{k_E\varepsilon^4}{2}\left[\sum_{\mu,\nu}(\tilde{l}^{\mu\nu})^2 + o(\varepsilon^0)\right] + k_S\left[\cos^{-1}\left(1 - \frac{\rho^2}{1/2\cos^2\gamma}\right) - \pi + 2\gamma + o(\varepsilon^0)\right]^2\right\}_{s=s_i} \\ &+ \sum_i \frac{k_F\varepsilon^2}{2}\left[\vartheta' + \frac{4[\rho^2 - (1/2\cos^2\gamma)](\tilde{l}^{1S} - \tilde{l}^{1D}) + (1/\cos\gamma)(\rho^2)' + (2/\cos^2\gamma)(\tilde{l}^{2D} - \tilde{l}^{2S})}{4\rho(1/2\cos\gamma)\sqrt{(1/\cos^2\gamma) - \rho^2}} + o(\varepsilon^0)\right]^2_{s=s_i} \\ &+ \sum_i \frac{k_F\varepsilon^2}{2}\left[\vartheta' + \frac{4[\rho^2 - (1/2\cos^2\gamma)](\tilde{l}^{2S} - \tilde{l}^{2D}) + (1/\cos\gamma)(\rho^2)' + (2/\cos^2\gamma)(\tilde{l}^{1D} - \tilde{l}^{1S})}{4\rho(1/2\cos\gamma)\sqrt{(1/\cos^2\gamma) - \rho^2}} + o(\varepsilon^0)\right]^2_{s=s_i}.\end{aligned} \tag{18}$$

Let the parameters $K_E, K_F, K_S > 0$ be constants, which do not depend on ε. Then they are related to the stiffnesses of each discrete system with micro length scale ε by a scaling law

$$k_E = K_E\varepsilon^{-3}, \quad k_F = K_F\varepsilon^{-1}, \quad k_S = K_S\varepsilon. \tag{19}$$

2.1.3. Pantographic beam: macro-model. The continuum limit is now obtained by letting $\varepsilon \to 0$. The deformation energy for the homogenized macro-model becomes

$$
\begin{aligned}
\mathcal{E} = & \int_0^L \left\{ K_S \left[\cos^{-1}\left(1 - \frac{\rho^2}{{}^1\!/_{2\cos^2\gamma}}\right) - \pi + 2\gamma \right]^2 + \frac{K_E}{2} \sum_{\mu\nu} \left(\tilde{l}^{\mu\nu}\right)^2 \right\} \mathrm{d}s \\
& + \int_0^L \frac{K_F}{2} \left[\vartheta' + \frac{4[\rho^2 - ({}^1\!/_{2\cos^2\gamma})](\tilde{l}^{1S} - \tilde{l}^{1D}) + ({}^1\!/_{\cos\gamma})(\rho^2)' + ({}^2\!/_{\cos^2\gamma})(\tilde{l}^{2D} - \tilde{l}^{2S})}{4\rho({}^1\!/_{2\cos\gamma})\sqrt{({}^1\!/_{\cos^2\gamma}) - \rho^2}} \right]^2 \mathrm{d}s \\
& + \int_0^L \frac{K_F}{2} \left[\vartheta' + \frac{4[\rho^2 - ({}^1\!/_{2\cos^2\gamma})](\tilde{l}^{2S} - \tilde{l}^{2D}) + ({}^1\!/_{\cos\gamma})(\rho^2)' + ({}^2\!/_{\cos^2\gamma})(\tilde{l}^{1D} - \tilde{l}^{1S})}{4\rho({}^1\!/_{2\cos\gamma})\sqrt{({}^1\!/_{\cos^2\gamma}) - \rho^2}} \right]^2 \mathrm{d}s.
\end{aligned}
\tag{20}
$$

The basic properties of the energy are preserved during the asymptotic process. Both the energy of the micro- and the macro-model (6) and (20), respectively, are invariant under superimposed rigid body motions. In addition, the extensional floppy mode of the discrete model, see (7), transfers to the continuum. Namely, if $\rho' = \vartheta' = \tilde{l}^{\mu\nu} = 0$ and $\rho(s) = 1$, then the deformation energy vanishes. When $K_S = 0$, if $\rho' = \vartheta' = \tilde{l}^{\mu\nu} = 0$, a constant stretch $\rho(s) = K \in (0, {}^1\!/_{\cos\gamma})$ can still be present without causing the deformation energy to be different from zero.

Let us now define the deformation energy density Ψ as the integrand of (20). For the energy to be stationary, the necessary conditions are obtained by equating to zero the variation of the deformation energy functional (20) with respect to admissible variations in the independent kinematic descriptors. At this stage, only the variation with respect to $\tilde{l}^{\mu\nu}$ is carried out. This results in a linear system of four algebraic equations given by $\partial\Psi/\partial\tilde{l}^{\mu\nu} = 0$ in which $\tilde{l}^{\mu\nu}$ are the unknowns. Introducing the abbreviations

$$
C_1 = \frac{K_F}{2K_F\rho^2 - {}^1\!/_{4\cos^2\gamma}(K_E\rho^2 + 8K_F)}, \quad C_2 = \frac{K_F\sqrt{{}^1\!/_{\cos^2\gamma} - \rho^2}}{K_E({}^1\!/_{4\cos^2\gamma})\rho^2 - 2K_F\rho^2 - 4K_E({}^1\!/_{16\cos^4\gamma})}, \tag{21}
$$

necessary conditions for equilibrium are that

$$
\tilde{l}^{\mu D} = \frac{1}{2\cos\gamma}\rho\left[\rho' C_1 + (-1)^{\mu-1}\vartheta' C_2\right], \quad \tilde{l}^{\mu S} = \frac{1}{2\cos\gamma}\rho\left[-\rho' C_1 + (-1)^{\mu}\vartheta' C_2\right]. \tag{22}
$$

By substituting the results (22) into (20), a kinematic reduction is performed resulting in the deformation energy functional of the pantographic beam

$$
\begin{aligned}
\mathcal{E} = \int_0^L \Bigg\{ & K_E K_F \left[\frac{\rho^2\cos^2\gamma - 1}{\rho^2\cos^2\gamma(K_E - 8K_F\cos^2\gamma) - K_E}\vartheta'^2 \right. \\
& \left. + \frac{\rho^2\cos^2\gamma}{(1 - \rho^2\cos^2\gamma)[8K_F + \rho^2(K_E - 8K_F\cos^2\gamma)]}\rho'^2 \right] + K_S\left[\cos^{-1}\left(1 - \frac{\rho^2}{{}^1\!/_{2\cos^2\gamma}}\right) - \pi + 2\gamma\right]^2 \Bigg\} \mathrm{d}s,
\end{aligned}
\tag{23}
$$

which merely depends on the placement function χ. The energy (23) is positive definite for $0 < \rho < 1/\cos\gamma$ and the complete second gradient χ'' of χ contributes to the deformation energy. In addition to the term $(\chi'_\perp \cdot \chi'')$ being related to the material curvature ϑ' by means of $(11)_1$, the term $(\chi' \cdot \chi'')$ also appears, which in turn is related to the stretch gradient ρ' given by $(23)_2$. It is also worth noting that, if $\rho(x) = 1/\cos\gamma$, then the term multiplying ϑ' in (23) vanishes. Consequently, at point $s = s_0$ the beam undergoes a beam-to-cable transition, being curvature no more energetically penalized. At the same time, if $\rho(s_0) = 1/\cos\gamma$, then the term multiplying ρ' in (23) diverges. Therefore, boundedness of energy requires $\rho'(s_0) = 0$.

2.2. Bi-pantographic fabrics: discrete model

The assembly of a discrete bi-pantographic fabric is sketched in Figure 2(b). The kinematics (and employed notation thereof) of discrete bi-pantographic fabrics is given by generalizing that of pantographic beams once the bi-pantographic structure is regarded as an assembly of two identical

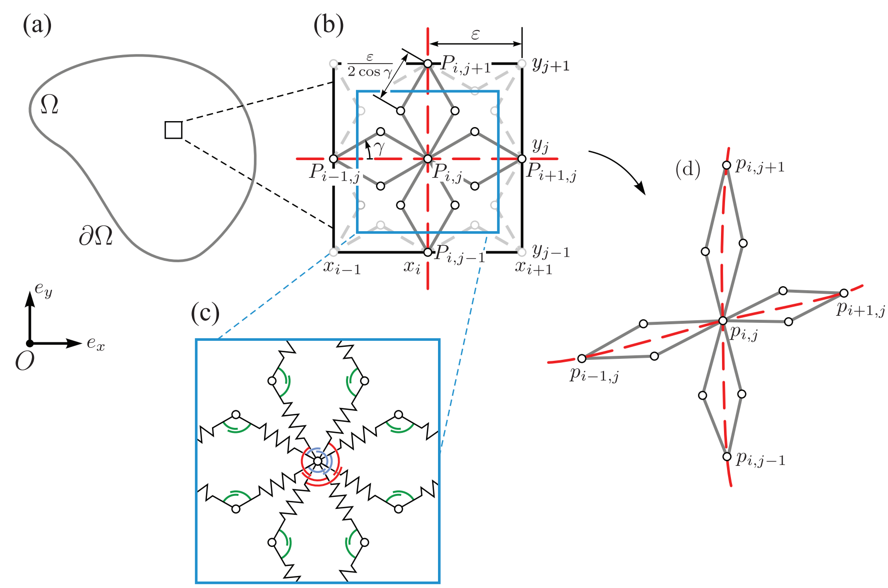

Figure 2. Bi-pantographic fabrics. (a) Domain Ω. (b) Undeformed configuration of the (i,j)th cell (including neighbouring elements). (c) Force elements of a single cell. (d) Deformed configuration of the (i,j)th cell (including neighbouring elements).

orthogonal families of parallel equispaced pantographic beams hinge-joined at their intersection points. Thus, aimed at avoiding unwieldy pictures, we omit to show it in Figure 2.

In the undeformed configuration, see Figure 2(a), cells are arranged within the reference domain Ω upon straight lines in direction of the unit basis vectors $e_x, e_y \in \mathbb{E}^2$. The set $\Omega \subseteq \mathbb{R}^2$ is in general a non-simple reference domain with boundary $\partial\Omega$ being the disjoint union of $N_\Omega \in \mathbb{N}$ smooth line sets $\partial\Omega_k$, $k \in [1; N_\Omega]$, pairwise intersecting in distinct vertices belonging to the set $[\partial\partial\Omega]$. A discussion on smoothness requirements for Ω is beyond the scope of this article. For such a discussion the reader is referred to [46]. The cells are centred at the positions $P_{i,j} = i\varepsilon e_x + j\varepsilon e_y$: see Figure 2(b). The basic (i,j)th unit cell (see Figure 2(c)) is formed by eight extensional springs hinge-joined together at $P_{i,j}$ having length $\varepsilon/(2\cos\gamma)$. Rotational springs, which are coloured in blue, red, and green in Figure 2(c), are placed between opposite collinear adjacent springs belonging to the same cell and between adjacent springs belonging to different cells.

The kinematics of the spring system is locally described by finitely many generalized coordinates. The coordinates are the positions $p_{i,j} \in \mathbb{E}^2$ of the points at position $P_{i,j}$ in the reference configuration (equivalently one can consider the nodal displacements $u_{i,j} \in \mathbb{R}^2$ such that $u_{i,j} = p_{i,j} - P_{i,j}$) and the lengths of the oblique deformed springs $l^{\mu\nu}_{(i,j),\alpha} \in \mathbb{R}$, $\alpha \in x, y$. The index α will be henceforth employed to distinguish quantities related to pantographic beams directed along e_x ($\alpha = x$) and e_y ($\alpha = y$). Various other kinematical quantities are introduced to formulate the total potential energy in a most compact form. Applying the law of cosines, the angles $\varphi^{\mu\nu}_{(i,j),\alpha}$ are determined by

$$
\begin{aligned}
\varphi^{1D}_{(i,j),x} &= \cos^{-1}\left[\frac{\| p_{i+1,j} - p_{i,j}\|^2 + \left(l^{1D}_{(i,j),x}\right)^2 - \left(l^{2S}_{(i+1,j),x}\right)^2}{2 l^{1D}_{(i,j),x} \| p_{i+1,j} - p_{i,j} \|}\right],\\
\varphi^{1S}_{(i,j),x} &= \cos^{-1}\left[\frac{\| p_{i,j} - p_{i-1,j}\|^2 + \left(l^{1S}_{(i,j),x}\right)^2 - \left(l^{2D}_{(i-1,j),x}\right)^2}{2 l^{1S}_{(i,j),x} \| p_{i,j} - p_{i-1,j} \|}\right],\\
\varphi^{2D}_{(i,j),x} &= \cos^{-1}\left[\frac{\| p_{i+1,j} - p_{i,j}\|^2 + \left(l^{2D}_{(i,j),x}\right)^2 - \left(l^{1S}_{(i+1,j),x}\right)^2}{2 l^{2D}_{(i,j),x} \| p_{i+1,j} - p_{i,j} \|}\right],\\
\varphi^{2S}_{(i,j),x} &= \cos^{-1}\left[\frac{\| p_{i,j} - p_{i-1,j}\|^2 + \left(l^{2S}_{(i,j),x}\right)^2 - \left(l^{1D}_{(i-1,j),x}\right)^2}{2 l^{2S}_{(i,j),x} \| p_{i,j} - p_{i-1,j} \|}\right],
\end{aligned}
\tag{24}
$$

and

$$
\begin{aligned}
\varphi^{1D}_{(i,j),y} &= \cos^{-1}\left[\frac{\| p_{i,j+1} - p_{i,j}\|^2 + (l^{1D}_{(i,j),y})^2 - (l^{2S}_{(i,j+1),y})^2}{2l^{1D}_{(i,j),y}\parallel p_{i,j+1} - p_{i,j}\parallel}\right],\\
\varphi^{1S}_{(i,j),y} &= \cos^{-1}\left[\frac{\| p_{i,j} - p_{i,j-1}\|^2 + (l^{1S}_{(i,j),y})^2 - (l^{2D}_{(i,j-1),y})^2}{2l^{1S}_{(i,j),y}\parallel p_{i,j} - p_{i,j-1}\parallel}\right],\\
\varphi^{2D}_{(i,j),y} &= \cos^{-1}\left[\frac{\| p_{i,j+1} - p_{i,j}\|^2 + (l^{2D}_{(i,j),y})^2 - (l^{1S}_{(i,j+1),y})^2}{2l^{2D}_{(i,j),y}\parallel p_{i,j+1} - p_{i,j}\parallel}\right],\\
\varphi^{2S}_{(i,j),y} &= \cos^{-1}\left[\frac{\| p_{i,j} - p_{i,j-1}\|^2 + (l^{2S}_{(i,j),y})^2 - (l^{1D}_{(i,j-1),x})^2}{2l^{2S}_{(i,j),y}\parallel p_{i,j} - p_{i,j-1}\parallel}\right],
\end{aligned}
\tag{25}
$$

while the angles $\xi^{\mu}_{(i,j),\alpha}$ become

$$
\begin{aligned}
\xi^{1(2)}_{(i,j),x} &= \cos^{-1}\left[\frac{(l^{1(2)D}_{(i,j),x})^2 + (l^{2(1)S}_{(i+1,j),x})^2 - \| p_{i+1,j} - p_{i,j}\|^2}{2l^{1(2)D}_{(i,j),x}l^{2(1)S}_{(i+1,j),x}}\right],\\
\xi^{1(2)}_{(i,j),y} &= \cos^{-1}\left[\frac{(l^{1(2)D}_{(i,j),y})^2 + (l^{2(1)S}_{(i,j+1),y})^2 - \| p_{i,j+1} - p_{i,j}\|^2}{2l^{1(2)D}_{(i,j),y}l^{2(1)S}_{(i,j+1),y}}\right].
\end{aligned}
\tag{26}
$$

Having used the law of cosines to determine $\varphi^{\mu\nu}_{(i,j),\alpha}$, the choice of generalized coordinates holds only locally as long as the angles $\varphi^{1D}_{(i,j),\alpha}$ and $\varphi^{2D}_{(i,j),\alpha}$ do not change sign. Throughout the derivation of the macro-model, it is assumed that the angles $\varphi^{1D}_{(i,j),\alpha}$ and $\varphi^{2D}_{(i,j),\alpha}$ remain in the range $(0,\pi)$. This entails that $\xi^{\mu}_{(i,j),\alpha} \in (0,\pi)$. The angle between the two vectors $p_{i,j} - p_{i-1,j}$ and e_x is denoted by $\vartheta_{(i,j),x}$, while the angle between the two vectors $p_{i,j} - p_{i,j-1}$ and e_y is denoted by $\vartheta_{(i,j),y}$. Then the angle $\theta_{(i,j),x}$ between the vectors $p_{i,j} - p_{i-1,j}$ and $p_{i+1,j} - p_{i,j}$ becomes

$$
\theta_{(i,j),x} = \vartheta_{(i+1,j),x} - \vartheta_{(i,j),x} = \tan^{-1}\left[\frac{(p_{i+1,j} - p_{i,j})\cdot e_y}{(p_{i+1,j} - p_{i,j})\cdot e_x}\right] - \tan^{-1}\left[\frac{(p_{i,j} - p_{i-1,j})\cdot e_y}{(p_{i,j} - p_{i-1,j})\cdot e_x}\right],
\tag{27}
$$

while the angle $\theta_{(i,j),y}$ between the vectors $p_{i,j} - p_{i,j-1}$ and $p_{i,j+1} - p_{i,j}$ reads

$$
\theta_{(i,j),y} = \vartheta_{(i,j+1),y} - \vartheta_{(i,j),y} = \tan^{-1}\left[\frac{(p_{i,j+1} - p_{i,j})\cdot e_y}{(p_{i,j+1} - p_{i,j})\cdot e_x}\right] - \tan^{-1}\left[\frac{(p_{i,j} - p_{i,j-1})\cdot e_y}{(p_{i,j} - p_{i,j-1})\cdot e_x}\right].
\tag{28}
$$

The following relations hold true

$$
\beta^1_{(i,j),\alpha} = \theta_{(i,j),\alpha} + \varphi^{1D}_{(i,j),\alpha} - \varphi^{1S}_{(i,j),\alpha}, \quad \beta^2_{(i,j),\alpha} = \theta_{(i,j),\alpha} + \varphi^{2S}_{(i,j),\alpha} - \varphi^{2D}_{(i,j),\alpha}.
\tag{29}
$$

Letting the summations for μ, ν and α range over the sets $\{1,2\}$, $\{D,S\}$ and $\{x,y\}$, respectively, and those for (i,j) over a set such that all energy contributions due to elastic elements in Ω are included in the subsequent formula, the micro-model deformation energy is defined as

$$\begin{aligned}\mathfrak{E}_\varepsilon &= \frac{k_E}{2}\sum_{i,j}\sum_{\alpha}\left[\sum_{\mu,\nu}\left(l^{\mu\nu}_{(i,j),\alpha}-\frac{1}{2\cos\gamma}\varepsilon\right)^2+\frac{k_F}{2}\sum_{\mu}\left(\beta^{\mu}_{(i,j),\alpha}\right)^2+\frac{k_S}{2}\sum_{\mu}(\xi^{\mu}_{(i,j),\alpha}-\pi+2\gamma)^2\right]\\ &\overset{(29)}{=}\frac{k_E}{2}\sum_{i,j}\sum_{\alpha}\left\{\sum_{\mu,\nu}\left(l^{\mu\nu}_{(i,j),\alpha}-\frac{1}{2\cos\gamma}\varepsilon\right)^2\right.\\ &\quad\left.+\frac{k_F}{2}\sum_{\mu}\left[\theta_{(i,j),\alpha}+(-1)^{\mu}\left(\varphi^{\mu S}_{(i,j),\alpha}-\varphi^{\mu D}_{(i,j),\alpha}\right)\right]^2+\frac{k_S}{2}\sum_{\mu}(\xi^{\mu}_{(i,j),\alpha}-\pi+2\gamma)^2\right\},\end{aligned} \tag{30}$$

with $k_E > 0$ and $k_F, k_S > 0$ being the stiffnesses of the extensional and rotational springs, respectively. The summand in (6) for the sum over (i,j) will be henceforth denoted by $\Psi_{i,j}$.

It is worth noting that, when $k_S = 0$, in addition to the rigid body modes also the set of admissible configurations obtained as all possible combinations of (1) uniform shear, i.e. the angle between the centrelines of the two families of pantographic beams is uniform and ranging from 0° to 180° (pantographic beams are transformed rigidly and, hence, this gives an infinite family of floppy modes parametrized on a single parameter that is the above-mentioned angle; when a bias rectangular specimen is considered, i.e. fibers form ±45° with the sides, this deformation mode corresponds to uniform extension/compression of the rectangle) and (2) extensional floppy mode of constituting pantographic beams entails null deformation energy. For more details on floppy modes in bi-pantographic structures the reader is referred to [35]. While each pantographic beam, as well as pantographic fabrics (whose only non-rigid zero energy deformation mode is given by uniform macroscopic shear; pantographic beams are replaced by (extensible) Elasticae that cannot extend with zero energy), admits an infinite family of extensional floppy modes parametrized over a single parameter (see Equation (7)), the bi-pantographic structure admits an infinite family of floppy modes parametrized over four parameters, see Figure 11 in [35].

For the lengths $l^{\mu\nu}_{(i,j),\alpha}$ of the oblique springs, the following asymptotic expansion is assumed

$$l^{\mu\nu}_{(i,j),\alpha} = \frac{1}{2\cos\gamma}\varepsilon + \varepsilon^2\tilde{l}^{\mu\nu}_{(i,j),\alpha} + o(\varepsilon^2), \tag{31}$$

where $\tilde{l}^{\mu\nu}_{(i,j),\alpha} \in \mathbb{R}$. Inserting assumption (31) into the energy (30) leads to

$$\begin{aligned}\mathfrak{E}_\varepsilon = \sum_{\alpha}\sum_{i,j}\left\{\frac{k_E}{2}\sum_{\mu,\nu}\left[\varepsilon^2\tilde{l}^{\mu\nu}_{(i,j),\alpha}+o(\varepsilon^2)\right]^2+\frac{k_F}{2}\sum_{\mu}\left[\theta_{(i,j),\alpha}+(-1)^{\mu}(\varphi^{\mu S}_{(i,j),\alpha}-\varphi^{\mu D}_{(i,j),\alpha})\right]^2\right.\\ \left.+\frac{k_S}{2}\sum_{\mu}(\xi^{\mu}_{(i,j),\alpha}-\pi+2\gamma)^2\right\}.\end{aligned} \tag{32}$$

2.3. Bi-pantographic fabrics: micro–macro identification

The two-dimensional extension of the discrete system makes it reasonable to aim for a two-dimensional continuum in the limit of vanishing ε. The independent kinematic Lagrangian descriptors of the macro-model are assumed to be the functions $\chi : \Omega \to \mathbb{E}^2$ and $\tilde{l}^{\mu\nu}_{\alpha} : \Omega \to \mathbb{R}$. The placement function χ places the 2D continuum into $\mathbb{E}^2$ and is best suited to describe the points $p_{i,j} \in \mathbb{E}^2$ of the discrete system on the macro-level. To take into account the effect of changing spring lengths $\tilde{l}^{\mu\nu}_{(i,j),\alpha}$ introduced in (8), the placement function is augmented by the eight micro-strain functions $\tilde{l}^{\mu\nu}_{\alpha}$. The identification of the discrete system with a 2D continuum is also classified as a micromorphic continuum [42-45].

It is also convenient to introduce the functions $\rho_\alpha : \Omega \to \mathbb{R}^+$ and $\vartheta_\alpha : \Omega \to [0, 2\pi)$ in order to rewrite the tangent vector field $\frac{\partial\chi}{\partial\alpha}$ to deformed material lines oriented along e_α in the reference configuration as

$$\begin{aligned}\frac{\partial\chi}{\partial x}(x,y) &= \rho_x(x,y)\{[\cos\vartheta_x(x,y)]e_x + [\sin\vartheta_x(x,y)]e_y\},\\ \frac{\partial\chi}{\partial y}(x,y) &= \rho_y(x,y)\{[\cos\vartheta_y(x,y)]e_y + [\sin\vartheta_y(x,y)]e_x\}.\end{aligned} \tag{33}$$

Thus, ρ_α corresponds to the norm of the tangent vector $\| {}^{\partial\chi}/_{\partial\alpha} \|$ to the deformed material lines directed along e_α in the reference configuration, and it is referred to as α-stretch. Introducing the normal vector fields to deformed material lines directed, respectively, along e_x and e_y in the reference configuration

$$\begin{aligned}\left(\frac{\partial\chi}{\partial x}\right)_\perp(x,y) &= \rho_x(x,y)\left\{-[\sin\vartheta_x(x,y)]e_x + [\cos\vartheta_x(x,y)]e_y\right\},\\ \left(\frac{\partial\chi}{\partial y}\right)_\perp(x,y) &= \rho_y(x,y)\left\{-\left[\sin\vartheta_y(x,y)\right]e_y + \left[\cos\vartheta_y(x,y)\right]e_x\right\},\end{aligned} \tag{34}$$

being respectively rotated against ${}^{\partial\chi}/_{\partial x}$ and ${}^{\partial\chi}/_{\partial y}$ about 90° in the anti-clockwise direction, it is found that

$$\begin{aligned}\frac{\partial\rho_x}{\partial x}(x,y) &= \frac{\frac{\partial\chi}{\partial x}(x,y)\cdot\frac{\partial^2\chi}{\partial x^2}(x,y)}{\|\frac{\partial\chi}{\partial x}(x,y)\|}, \quad & \frac{\partial\vartheta_x}{\partial x}(x,y) &= \frac{\frac{\partial^2\chi}{\partial x^2}(x,y)\cdot\left(\frac{\partial\chi}{\partial x}\right)_\perp(x,y)}{\|\frac{\partial\chi}{\partial x}(x,y)\|^2},\\ \frac{\partial\rho_y}{\partial y}(x,y) &= \frac{\frac{\partial\chi}{\partial y}(x,y)\cdot\frac{\partial^2\chi}{\partial y^2}(x,y)}{\|\frac{\partial\chi}{\partial y}(x,y)\|}, \quad & \frac{\partial\vartheta_y}{\partial y}(x,y) &= \frac{\frac{\partial^2\chi}{\partial y^2}(x,y)\cdot\left(\frac{\partial\chi}{\partial y}\right)_\perp(x,y)}{\|\frac{\partial\chi}{\partial y}(x,y)\|^2}.\end{aligned} \tag{35}$$

In the following ${}^{\partial\rho_\alpha}/_{\partial\alpha}$ and ${}^{\partial\vartheta_\alpha}/_{\partial\alpha}$ are called α-stretch α-derivative and material α-curvature, respectively. For Piola's micro–macro identification the generalized coordinates of the discrete system are related to the functions χ and $\tilde{l}^{\mu\nu}_\alpha$ evaluated at $(x_i, y_j) = (i\varepsilon, j\varepsilon)$ as

$$\chi(x_i, y_j) = p_{i,j}, \quad \tilde{l}^{\mu\nu}_\alpha(x_i, y_j) = \tilde{l}^{\mu\nu}_{(i,j),\alpha}. \tag{36}$$

For the asymptotic identification, the energy (32) needs to be expanded in ε. The expansion of χ is given by

$$\begin{aligned}\chi(x_{i\pm1}, y_j) &= \chi(x_i, y_j) \pm \varepsilon\frac{\partial\chi}{\partial x}(x_i, y_j) + \frac{\varepsilon^2}{2}\frac{\partial^2\chi}{\partial x^2}(x_i, y_j) + o(\varepsilon^2),\\ \chi(x_i, y_{j\pm1}) &= \chi(x_i, y_j) \pm \varepsilon\frac{\partial\chi}{\partial y}(x_i, y_j) + \frac{\varepsilon^2}{2}\frac{\partial^2\chi}{\partial y^2}(x_i, y_j) + o(\varepsilon^2).\end{aligned} \tag{37}$$

Combining the asymptotic expansion (31) with $(36)_2$, $\tilde{l}^{\mu\nu}_x(x_{i\pm1}, y_j) = \tilde{l}^{\mu\nu}_x(x_i, y_j) + o(\varepsilon^0)$ and $\tilde{l}^{\mu\nu}_y(x_i, y_{j\pm1}) = \tilde{l}^{\mu\nu}_y(x_i, y_j) + o(\varepsilon^0)$, yields

$$\begin{aligned}l^{\mu\nu}_{(i\pm1,j),x} &= \tfrac{1}{2\cos\gamma}\varepsilon + \tilde{l}^{\mu\nu}_x(x_i, y_j)\varepsilon^2 + o(\varepsilon^2),\\ l^{\mu\nu}_{(i,j\pm1),y} &= \tfrac{1}{2\cos\gamma}\varepsilon + \tilde{l}^{\mu\nu}_y(x_i, y_j)\varepsilon^2 + o(\varepsilon^2).\end{aligned} \tag{38}$$

In order to further expand (32), the terms $\theta_{(i,j),\alpha}$, $\varphi^{\mu S}_{(i,j),\alpha} - \varphi^{\mu D}_{(i,j),\alpha}$ and $\xi^\mu_{(i,j),\alpha}$ need to be expanded up to first order (see Appendix 6). For $\theta_{(i,j),\alpha}$ according to (71)

$$\theta_{(i,j),\alpha} = \varepsilon\frac{\partial\vartheta_{(i,j),\alpha}}{\partial\alpha}(x_i, y_j) + o(\varepsilon). \tag{39}$$

The differences $\varphi^{1(2)S}_{(i,j),\alpha} - \varphi^{1(2)D}_{(i,j),\alpha}$ are given by (78) as

$$\varphi^{1(2)S}_{(i,j),\alpha} - \varphi^{1(2)D}_{(i,j),\alpha} = \left.\frac{4\left[\rho_\alpha^2 - ({}^1/_{2\cos^2\gamma})\right](\tilde{l}^{1(2)S}_\alpha - \tilde{l}^{1(2)D}_\alpha) + ({}^1/_{\cos\gamma}\frac{\partial(\rho_\alpha^2)}{\partial\alpha}) + ({}^2/_{\cos^2\gamma})(\tilde{l}^{2(1)D}_\alpha - \tilde{l}^{2(1)S}_\alpha)}{4\rho_\alpha({}^1/_{2\cos\gamma})\sqrt{({}^1/_{\cos^2\gamma}) - \rho_\alpha^2}}\right|_{(x,y)=(x_i,y_j)} \varepsilon + o(\varepsilon). \tag{40}$$

The angles $\xi^\mu_{(i,j),\alpha}$ are given by (80) as

$$\xi^{\mu}_{(i,j),\alpha} = \cos^{-1}\left(1 - \frac{\rho_\alpha^2}{{}^1\!/_2\cos^2\gamma}\right)\bigg|_{(x,y)=(x_i,y_j)} + o(\varepsilon^0). \tag{41}$$

Substituting (39), (40) and (41) into (32) together with $\rho_\alpha(x_i,y_j) = \parallel \frac{\partial\chi}{\partial\alpha} \parallel$, the desired expansion of the micro-model energy $\mathfrak{E}_\varepsilon$ is derived as a function of the kinematic descriptors χ and $\tilde{l}^{\mu\nu}_\alpha$ as

$$\begin{aligned}\mathfrak{E}_\varepsilon = &\sum_{i,j}\sum_\alpha \left\{\frac{k_E\varepsilon^4}{2}\left[\sum_{\mu,\nu}(\tilde{l}^{\mu\nu}_\alpha)^2 + o(\varepsilon^0)\right] + k_S\left[\cos^{-1}\left(1-\frac{\rho_\alpha^2}{{}^1\!/_2\cos^2\gamma}\right) - \pi + 2\gamma + o(\varepsilon^0)\right]^2\right\}_{(x,y)=(x_i,y_j)}\\ &+ \sum_{i,j}\sum_\alpha \frac{k_F\varepsilon^2}{2}\left[\frac{\partial\vartheta}{\partial\alpha} + \frac{4[\rho_\alpha^2 - ({}^1\!/_2\cos^2\gamma)](\tilde{l}^{1S}_\alpha - \tilde{l}^{1D}_\alpha) + ({}^1\!/_{\cos\gamma})\frac{\partial(\rho_\alpha^2)}{\partial\alpha} + ({}^2\!/_{\cos^2\gamma})(\tilde{l}^{2D}_\alpha - \tilde{l}^{2S}_\alpha)}{4\rho_\alpha({}^1\!/_2\cos\gamma)\sqrt{({}^1\!/_{\cos^2\gamma}) - \rho_\alpha^2}} + o(\varepsilon^0)\right]^2_{(x,y)=(x_i,y_j)}\\ &+ \sum_{i,j}\sum_\alpha \frac{k_F\varepsilon^2}{2}\left[\frac{\partial\vartheta}{\partial\alpha} + \frac{4[\rho_\alpha^2 - ({}^1\!/_2\cos^2\gamma)](\tilde{l}^{2S}_\alpha - \tilde{l}^{2D}_\alpha) + ({}^1\!/_{\cos\gamma})\frac{\partial(\rho_\alpha^2)}{\partial\alpha} + ({}^2\!/_{\cos^2\gamma})(\tilde{l}^{1D}_\alpha - \tilde{l}^{1S}_\alpha)}{4\rho_\alpha({}^1\!/_2\cos\gamma)\sqrt{({}^1\!/_{\cos^2\gamma}) - \rho_\alpha^2}} + o(\varepsilon^0)\right]^2_{(x,y)=(x_i,y_j)}.\end{aligned} \tag{42}$$

Let the parameters $K_E, K_F, K_S > 0$ be constants, which do not depend on ε. Then these constants are related to the stiffnesses of each discrete system with micro length scale ε by a scaling law

$$k_E = K_E\varepsilon^{-2}, \quad k_F = K_F, \quad k_S = K_S\varepsilon^2. \tag{43}$$

2.4. Bi-pantographic fabrics: macro-model

The continuum limit is now obtained by letting $\varepsilon \to 0$ and considering the sum to turn into an integral according to $\sum_{i,j} f(x_i,y_j)\varepsilon^2 \overset{\varepsilon\to 0}{\to} \int_\Omega f\, dA$, where f is a real-valued function defined on Ω. Using (42) together with the scaling law (43), the deformation energy for the homogenized macro-model becomes

$$\begin{aligned}\mathfrak{E} = &\int_\Omega \sum_\alpha \left\{\frac{K_E}{2}\left[\sum_{\mu,\nu}(\tilde{l}^{\mu\nu}_\alpha)^2\right] + K_S\left[\cos^{-1}\left(1-\frac{\rho_\alpha^2}{{}^1\!/_2\cos^2\gamma}\right) - \pi + 2\gamma\right]^2\right\}\mathrm{d}A\\ &+ \int_\Omega \sum_\alpha \frac{K_F}{2}\left[\frac{\partial\vartheta_\alpha}{\partial\alpha} + \frac{4[\rho_\alpha^2 - ({}^1\!/_2\cos^2\gamma)](\tilde{l}^{1S}_\alpha - \tilde{l}^{1D}_\alpha) + ({}^1\!/_{\cos\gamma})\frac{\partial(\rho_\alpha^2)}{\partial\alpha} + ({}^2\!/_{\cos^2\gamma})(\tilde{l}^{2D}_\alpha - \tilde{l}^{2S}_\alpha)}{4\rho_\alpha({}^1\!/_2\cos\gamma)\sqrt{({}^1\!/_{\cos^2\gamma}) - \rho_\alpha^2}}\right]^2\mathrm{d}A\\ &+ \int_\Omega \sum_\alpha \frac{K_F}{2}\left[\frac{\partial\vartheta_\alpha}{\partial\alpha} + \frac{4[\rho_\alpha^2 - ({}^1\!/_2\cos^2\gamma)](\tilde{l}^{2S}_\alpha - \tilde{l}^{2D}_\alpha) + ({}^1\!/_{\cos\gamma})\frac{\partial(\rho_\alpha^2)}{\partial\alpha} + ({}^2\!/_{\cos^2\gamma})(\tilde{l}^{1D}_\alpha - \tilde{l}^{1S}_\alpha)}{4\rho_\alpha({}^1\!/_2\cos\gamma)\sqrt{({}^1\!/_{\cos^2\gamma}) - \rho_\alpha^2}}\right]^2\mathrm{d}A.\end{aligned} \tag{44}$$

Considerations on the above-derived continuum limit analogous to those made in the previous subsection dealing with preliminary computations can be invoked. The above deformation energy is objective and discrete floppy modes transfer to the continuum after homogenization. The above deformation energy is vanishing for $\chi(x,y) = [x + (ay+b)x]e_x + [y + (cy+d)x]e_y$ (see [35]) when $K_S = 0$. When $a = c = d = 0$, then χ represents uniform extension, while when $a = c = 0$ it describes uniform shear deformation, which is the only non-rigid zero energy deformation mode for pantographic fabrics [11]. The derived continuum limit, as for pantographic fabrics, inherits its orthotropicity from its fibred structure at the micro-scale, i.e. it can be regarded as made by assembling two identical orthogonal families of (equispaced) parallel discrete pantographic beams. Let us now define the deformation energy density Ψ as the integrand of (44). For the energy to be stationary, the necessary conditions are obtained by equating to zero the variation of the deformation energy functional (44) with respect to admissible variations in the independent kinematic descriptors. First, only the variation with respect to $\tilde{l}^{\mu\nu}_\alpha$ is studied, and results in a linear system of eight algebraic equations given by $\partial\Psi/\partial\tilde{l}^{\mu\nu}_\alpha = 0$ in which $\tilde{l}^{\mu\nu}_\alpha$ are the unknowns. Introducing the notation

$$C_1^\alpha = \frac{K_F}{2K_F\rho_\alpha^2 - {}^1\!/_{4\cos^2\gamma}\left(K_E\rho_\alpha^2 + 8K_F\right)}, \quad C_2^\alpha = \frac{K_F\sqrt{{}^1\!/_{\cos^2\gamma} - \rho_\alpha^2}}{K_E({}^1\!/_{4\cos^2\gamma})\rho_\alpha^2 - 2K_F\rho_\alpha^2 - 4K_E({}^1\!/_{16\cos^4\gamma})}, \tag{45}$$

necessary conditions for equilibrium are that

$$\tilde{l}_\alpha^{\mu D} = \frac{1}{2\cos\gamma}\rho_\alpha\left[\frac{\partial\rho_\alpha}{\partial\alpha}C_1^\alpha + (-1)^{\mu-1}\frac{\partial\vartheta_\alpha}{\partial\alpha}C_2^\alpha\right], \qquad \tilde{l}_\alpha^{\mu S} = \frac{1}{2\cos\gamma}\rho_\alpha\left[-\frac{\partial\rho_\alpha}{\partial\alpha}C_1^\alpha + (-1)^{\mu}\frac{\partial\vartheta_\alpha}{\partial\alpha}C_2^\alpha\right]. \tag{46}$$

By substituting the results (46) into (44), a kinematic reduction is performed and results in the deformation energy functional of the bi-pantographic structure

$$\begin{aligned}\mathfrak{E} = \int_\Omega \sum_\alpha \Bigg\{ & K_E K_F \left[\frac{\rho_\alpha^2\cos^2\gamma - 1}{\rho_\alpha^2\cos^2\gamma(K_E - 8K_F\cos^2\gamma) - K_E}\left(\frac{\partial\vartheta_\alpha}{\partial\alpha}\right)^2\right. \\ & \left. + \frac{\rho_\alpha^2\cos^2\gamma}{\left(1-\rho_\alpha^2\cos^2\gamma\right)\left[8K_F + \rho_\alpha^2(K_E - 8K_F\cos^2\gamma)\right]}\left(\frac{\partial\rho_\alpha}{\partial\alpha}\right)^2\right] + K_S\left[\cos^{-1}\left(1 - \frac{\rho_\alpha^2}{{}^1\!/_{2\cos^2\gamma}}\right) - \pi + 2\gamma\right]^2\Bigg\}\mathrm{d}A\end{aligned} \tag{47}$$

which depends on the placement function χ only. Note that, in addition to the term $\left(\frac{\partial\chi}{\partial\alpha}\right)_\perp \cdot \frac{\partial^2\chi}{\partial\alpha^2}$ being related to the material α-curvature $\frac{\partial\vartheta_\alpha}{\partial\alpha}$ by means of (35), also the term $\frac{\partial\chi}{\partial\alpha}\cdot\frac{\partial^2\chi}{\partial\alpha^2}$ appears, which, in turn, is related to the α-stretch α-derivative $\frac{\partial\rho_\alpha}{\partial\alpha}$ given by Equation (35).

A detailed derivation of Euler–Lagrange equations, essential and natural boundary conditions (BCs) as deduced from stationarity condition for energy functionals of the form $\int_\Omega W(\nabla\chi, \nabla\nabla\chi)\mathrm{d}A$, as that in (47), is beyond the scope of this article, and the reader is referred to [46]. However, it is worth recalling that in such a case non-classical essential normal placement gradient BCs, i.e. prescribing $\nabla\chi(x,y)\cdot n(x,y) = f(x,y)$, can be given at boundaries $\partial\Omega_k$, n being the outwards pointing unit normal, and essential placement BC's, i.e. prescribing $\chi(x,y) = g(x,y)$, can be given at vertices belonging to $[\partial\partial\Omega]$, in addition to classical essential placement BCs at boundaries $\partial\Omega_k$.

2.5. Bi-pantographic fabrics: linearization of deformation energy

Let the vector-valued displacement field u be defined by $u(x,y) = \chi(x,y) - xe_x - ye_y$. Then by the Piola's identification (36) and by the definition of nodal displacements $u_{i,j}$ we have $u(x_i, y_j) = u_{i,j}$. From Taylor expansions it follows that

$$\begin{aligned}\vartheta_x &= \tan^{-1}\left[\frac{\partial u}{\partial x}\cdot e_y\Big/\left(1 + \frac{\partial u}{\partial x}\cdot e_x\right)\right] = \frac{\partial u}{\partial x}\cdot e_y + o\left(\left\|\frac{\partial u}{\partial x}\right\|\right) = o\left(\left\|\frac{\partial u}{\partial x}\right\|^0\right), \\ \vartheta_y &= \tan^{-1}\left[\frac{\partial u}{\partial y}\cdot e_x\Big/\left(1 + \frac{\partial u}{\partial y}\cdot e_y\right)\right] = \frac{\partial u}{\partial y}\cdot e_x + o\left(\left\|\frac{\partial u}{\partial y}\right\|\right) = o\left(\left\|\frac{\partial u}{\partial y}\right\|^0\right),\end{aligned} \tag{48}$$

and, therefore,

$$\frac{\partial\vartheta_x}{\partial x} = \frac{\partial^2 u}{\partial x^2}\cdot e_y + o\left(\left\|\frac{\partial u}{\partial x}\right\|^0\right), \quad \frac{\partial\vartheta_y}{\partial y} = \frac{\partial^2 u}{\partial y^2}\cdot e_x + o\left(\left\|\frac{\partial u}{\partial y}\right\|^0\right). \tag{49}$$

Moreover,

$$\begin{aligned}\rho_x &= \left[\left(1 + \frac{\partial u}{\partial x}\cdot e_x\right)^2 + \left(\frac{\partial u}{\partial x}\cdot e_y\right)^2\right]^{\frac{1}{2}} = 1 + \frac{\partial u}{\partial x}\cdot e_x + o\left(\left\|\frac{\partial u}{\partial x}\right\|\right) = 1 + o\left(\left\|\frac{\partial u}{\partial x}\right\|^0\right), \\ \rho_y &= \left[\left(1 + \frac{\partial u}{\partial y}\cdot e_y\right)^2 + \left(\frac{\partial u}{\partial y}\cdot e_x\right)^2\right]^{\frac{1}{2}} = 1 + \frac{\partial u}{\partial y}\cdot e_y + o\left(\left\|\frac{\partial u}{\partial y}\right\|\right) = 1 + o\left(\left\|\frac{\partial u}{\partial y}\right\|^0\right),\end{aligned} \tag{50}$$

and, thus,

$$\frac{\partial \rho_\alpha}{\partial \alpha} = \frac{\partial^2 u}{\partial \alpha^2} \cdot e_\alpha + o\left(\left\| \frac{\partial u}{\partial \alpha} \right\|^0 \right). \tag{51}$$

Hence, the energy (47) rewrites as (see Equation (85) in Appendix A)

$$\begin{aligned} \mathfrak{E} = & \int_\Omega \left\{ \left[\frac{K_E K_F \cos^2 \gamma}{(1-\cos^2\gamma)[8K_F + K_E - 8K_F \cos^2 \gamma]} \right] \left[\left(\frac{\partial^2 u}{\partial x^2} \cdot e_x \right)^2 + \left(\frac{\partial^2 u}{\partial y^2} \cdot e_y \right)^2 \right] \right\} \mathrm{d}A \\ & + \int_\Omega \left\{ \left[\frac{K_E K_F (\cos^2\gamma - 1)}{\cos^2\gamma (K_E - 8K_F \cos^2 \gamma) - K_E} \right] \left[\left(\frac{\partial^2 u}{\partial x^2} \cdot e_y \right)^2 + \left(\frac{\partial^2 u}{\partial y^2} \cdot e_x \right)^2 \right] \right\} \mathrm{d}A \\ & + \int_\Omega \left\{ \sum_\alpha [4K_S \cot\gamma] \left(\frac{\partial u}{\partial \alpha} \cdot e_\alpha \right)^2 + o\left(\left\| \frac{\partial u}{\partial \alpha} \right\|^2 \right) \right\} \mathrm{d}A. \end{aligned} \tag{52}$$

For the small strain hypothesis the remainder $o(\| \partial u/\partial \alpha \|^2)$ in Equation (52) can be neglected.

3. Computational aspects

In this section, the problem to be solved is introduced and solution methodologies employed for the macro- and micro-model are briefly recalled.

3.1. Boundary value problem (non-standard bias extension test)

A rectangular specimen, i.e. $N_\Omega = 4$, with sides $L = 187$ mm $\times$ $\ell = 119$ mm and $\varepsilon = 12.02$ mm is considered, see Figure 3. The geometric parameter γ is assumed to be equal to $\pi/6$. The following essential BCs are considered

$$\begin{aligned} & u(x,y) = 0 \quad \text{at } (x,y) \in \partial\Omega_1, \quad u(x,y) = \bar{u} e_\zeta \quad \text{at } (x,y) \in \partial\Omega_3, \quad \bar{u} \in \mathbb{R} \\ & [\nabla u(x,y)] n(x,y) = 0 \quad \text{at } (x,y) \in \partial\Omega_1, \quad [\nabla u(x,y)] n(x,y) = 0 \quad \text{at } (x,y) \in \partial\Omega_3 \end{aligned} \tag{53}$$

which do not entail a floppy deformation mode. As the displacement field $u(x,y)$ is enforced to be constant along the boundaries $\partial\Omega_1$ and $\partial\Omega_3$, then $[\nabla u(x,y)] n_\perp(x,y)$ is also vanishing along those boundaries. This, together with $(53)_2$, implies that

$$\nabla u(x,y) = 0 \quad \text{at } (x,y) \in \partial\Omega_1 \cup \partial\Omega_3 \tag{54}$$

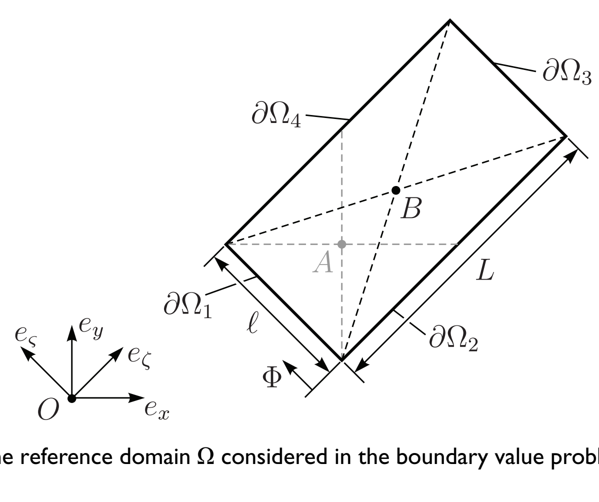

Figure 3. Schematic drawing of the reference domain Ω considered in the boundary value problem for the macro-model.

Equation (54) is equivalent to

$$\rho_\alpha(x,y) = 1 \quad \text{at } (x,y) \in \partial\Omega_1 \cup \partial\Omega_3, \quad \vartheta_\alpha(x,y) = 0 \quad \text{at } (x,y) \in \partial\Omega_1 \cup \partial\Omega_3. \tag{55}$$

To compare the micro- and macro-model, beyond the micro–macro identification (12), the following micro–macro correspondences, based on neglecting non-leading ε-terms in Taylor expansions of continuum quantities evaluated at discrete points, shall be taken into account. For stretches and orientations of pantographic beams

$$\begin{aligned} \rho_x(x_i, y_i) &\leftrightarrow \frac{\| p_{i+1,j} - p_{i,j} \|}{\varepsilon}, \quad \vartheta_x(x_i, y_j) \leftrightarrow \vartheta_{i,j} = \tan^{-1}\left[\frac{(p_{i,j} - p_{i-1,j}) \cdot e_y}{(p_{i,j} - p_{i-1,j}) \cdot e_x}\right] \\ \rho_y(x_i, y_j) &\leftrightarrow \frac{\| p_{i,j+1} - p_{i,j} \|}{\varepsilon}, \quad \vartheta_y(x_i, y_j) \leftrightarrow \vartheta_{i,j} = \tan^{-1}\left[\frac{(p_{i,j} - p_{i,j-1}) \cdot e_x}{(p_{i,j} - p_{i,j-1}) \cdot e_y}\right]. \end{aligned} \tag{56}$$

In addition, the micro-strains $\tilde{l}_\alpha^{\mu\nu}$ are related by

$$\tilde{l}_\alpha^{\mu\nu}(x_i, y_j) \leftrightarrow \frac{l_{(i,j),\alpha}^{\mu\nu}}{\varepsilon}. \tag{57}$$

The deformation energy density $\Psi(x,y)$, which is the integrand of (47), is compared by the following relation

$$\Psi(x_i, y_j) \leftrightarrow \Psi_{i,j}. \tag{58}$$

The shear angle is compared by the following relation

$$\left[\pi/2 - \arccos\left(\frac{\nabla\chi\, e_x \cdot \nabla\chi\, e_y}{\| \nabla\chi\, e_x \| \| \nabla\chi\, e_y \|}\right)\right]_{(x,y)=(x_i,y_j)} \leftrightarrow \pi/2 - \arccos\left[\frac{(p_{i+1,j} - p_{i,j}) \cdot (p_{i,j+1} - p_{i,j})}{\| p_{i+1,j} - p_{i,j} \| \| p_{i,j+1} - p_{i,j} \|}\right]. \tag{59}$$

Last, in an analogous fashion the following micro–macro correspondences are defined on boundaries

$$\begin{aligned} &\frac{\partial u}{\partial x}(x_i, y_j) \leftrightarrow \frac{u_{i+1,j} - u_{i,j}}{\varepsilon} \quad \text{and} \quad \frac{\partial u}{\partial y}(x_i, y_j) \leftrightarrow \frac{u_{i,j+1} - u_{i,j}}{\varepsilon} \quad \text{for all } (x_i, y_j) \in \partial\Omega_1 \\ &\frac{\partial u}{\partial x}(x_i, y_j) \leftrightarrow \frac{u_{i,j} - u_{i-1,j}}{\varepsilon} \quad \text{and} \quad \frac{\partial u}{\partial y}(x_i, y_j) \leftrightarrow \frac{u_{i,j} - u_{i,j-1}}{\varepsilon} \quad \text{for all } (x_i, y_j) \in \partial\Omega_3 \end{aligned} \tag{60}$$

which, together with Piola's micro–macro identification (36), are used to establish a correspondence between BCs (53) for the continuum model and those for the discrete one. Such a correspondence is reported in Table 1.

3.2. Macro-model: finite element formulation

A mixed finite element formulation is adopted for the solution of the macro-model. Let us define the following augmented energy functional

Table 1. BCs for the micro- and macro-model.

Micro-model	Macro-model
$u_{i,j} = 0$ for all (i,j) s.t. $(x_i, y_j) \in \partial\Omega_1$	$u(x,y) = 0$ for all $(x,y) \in \partial\Omega_1$
$u_{i,j} = \bar{u}e_\zeta$ for all (i,j) s.t. $(x_i, y_j) \in \partial\Omega_3$	$u(x,y) = \bar{u}e_\zeta$ for all $(x,y) \in \partial\Omega_3$
$u_{i+1,j} = u_{i,j}$ for all (i,j) s.t. $(x_i, y_j) \in \partial\Omega_1$	$[\nabla u(x,y)]n(x,y) = 0$ for all $(x,y) \in \partial\Omega_1 \cup \Omega_3$
$u_{i,j+1} = u_{i,j}$ for all (i,j) s.t. $(x_i, y_j) \in \partial\Omega_1$	
$u_{i-1,j} = u_{i,j}$ for all (i,j) s.t. $(x_i, y_j) \in \partial\Omega_3$	
$u_{i,j-1} = u_{i,j}$ for all (i,j) s.t. $(x_i, y_j) \in \partial\Omega_3$	

$$
\begin{aligned}
\tilde{\mathfrak{E}} = & \sum_{k=1}^{N_\Omega} \int_{\partial\Omega_k} \sum_{\alpha} \{\mu_\alpha \cdot [(\nabla u - M) n_\perp]\} \mathrm{d}A + \int_\Omega \sum_\alpha \{\lambda_\alpha \cdot \left(M e_\alpha - \frac{\partial u}{\partial \alpha} \right) \\
& + K_E K_F [\frac{(\rho_\alpha^2 \cos^2\gamma - 1)[\kappa_\alpha(M)]^2}{\rho_\alpha^2 \cos^2\gamma (K_E - 8K_F \cos^2\gamma) - K_E} \\
& + \frac{(\rho_\alpha^2 \cos^2\gamma)[\iota_\alpha(M)]}{(1 - \rho_\alpha^2 \cos^2\gamma)\left[8K_F + \rho_\alpha^2 (K_E - 8K_F \cos^2\gamma)\right]}] + K_S \left[\cos^{-1}\left(1 - \frac{\rho_\alpha^2}{{}^1\!/_2 \cos^2\gamma} \right) - \pi + 2\gamma \right]^2 \} \mathrm{d}A \\
& + \int_{\partial\Omega_1 \cup \partial\Omega_3} (\eta \cdot [\nabla u] n) \mathrm{d}l + \int_{\partial\Omega_1} (\gamma \cdot u) \mathrm{d}l + \int_{\partial\Omega_3} [\upsilon \cdot (u - \bar{u} e_\zeta)] \mathrm{d}l.
\end{aligned}
\tag{61}
$$

where M is an independent auxiliary field that is weakly enforced by Lagrange multipliers μ_α and λ_α to be equal to ∇u [47], and

$$
\begin{aligned}
\kappa_x(M) &= \frac{\frac{\partial(Me_x)}{\partial x} \cdot \left[\left(1 + \frac{\partial u}{\partial x} \cdot e_x, \frac{\partial u}{\partial x} \cdot e_y\right)^{\mathrm{T}}\right]_\perp}{\| \left(1 + \frac{\partial u}{\partial x} \cdot e_x, \frac{\partial u}{\partial x} \cdot e_y\right)^{\mathrm{T}} \|^2}, \qquad \iota_x(M) = \frac{\frac{\partial(Me_x)}{\partial x} \cdot \left(1 + \frac{\partial u}{\partial x} \cdot e_x, \frac{\partial u}{\partial x} \cdot e_y\right)^{\mathrm{T}}}{\| \left(1 + \frac{\partial u}{\partial x} \cdot e_x, \frac{\partial u}{\partial x} \cdot e_y\right)^{\mathrm{T}} \|} \\
\kappa_y(M) &= \frac{\frac{\partial(Me_y)}{\partial y} \cdot \left[\left(1 + \frac{\partial u}{\partial y} \cdot e_y, \frac{\partial u}{\partial y} \cdot e_x\right)^{\mathrm{T}}\right]_\perp}{\| \left(1 + \frac{\partial u}{\partial y} \cdot e_y, \frac{\partial u}{\partial y} \cdot e_x\right)^{\mathrm{T}} \|^2}, \qquad \iota_y(M) = \frac{\frac{\partial(Me_y)}{\partial y} \cdot \left(1 + \frac{\partial u}{\partial y} \cdot e_y, \frac{\partial u}{\partial y} \cdot e_x\right)^{\mathrm{T}}}{\| \left(1 + \frac{\partial u}{\partial y} \cdot e_y, \frac{\partial u}{\partial y} \cdot e_x\right)^{\mathrm{T}} \|}
\end{aligned}
\tag{62}
$$

are α-curvature (κ_α) and α-stretch α-derivative (ι_α) expressed in terms of only the first spatial derivatives of the independent fields u and M. In such a way, the deformation energy (47) can be transformed into an augmented energy functional written in terms of first spatial derivatives of the independent kinematic quantities. The discretization of these quantities by the finite element method to solve the stationarity condition of such augmented energy functional does not require C^1-continuous shape functions such as those needed to solve the stationarity condition for the energy (47) in terms of the only unknown field u. Let $\tilde{\Psi}$ be the argument of integration over Ω in (61). Let $\tilde{\Psi}_k$ be the argument of integration over $\partial\Omega_k$ in (61). From the stationarity condition for the energy (61) is determined the weak form

$$
\begin{aligned}
0 = & \sum_\alpha \sum_{k=1}^{N_\Omega} \int_{\partial\Omega_k} \left[\frac{\partial \tilde{\Psi}_k}{\partial(\partial u/\partial\alpha)} \cdot \delta\left(\frac{\partial u}{\partial \alpha}\right) + \frac{\tilde{\Psi}_k}{\partial(Me_\alpha)} \cdot \delta(Me_\alpha) + \frac{\partial\tilde{\Psi}_k}{\partial\mu_\alpha} \cdot \delta\mu_\alpha \right] \mathrm{d}l \\
& + \sum_\alpha \int_\Omega \left[\frac{\partial\tilde{\Psi}}{\partial(\partial u/\partial\alpha)} \cdot \delta\left(\frac{\partial u}{\partial\alpha}\right) + \frac{\partial\tilde{\Psi}}{\partial(Me_\alpha)} \cdot \delta(Me_\alpha) + \frac{\partial\tilde{\Psi}}{\partial\lambda_\alpha} \cdot \delta\lambda_\alpha \right] \mathrm{d}A \\
& + \sum_{k=1}^{N_\Omega} \int_{\partial\Omega_k} \left[\frac{\partial\tilde{\Psi}_k}{\partial\eta} \cdot \delta\eta + \frac{\partial\tilde{\Psi}_k}{\partial\gamma} \cdot \delta\gamma + \frac{\partial\tilde{\Psi}_k}{\partial\upsilon} \cdot \delta\upsilon \right] \mathrm{d}l,
\end{aligned}
\tag{63}
$$

where $\delta(\cdot)$ denotes the kinematically admissible variation of $(\cdot)$, which can then be solved numerically by a finite element code. The *weak form* package of the software COMSOL Multiphysics, which implements standard finite element techniques [48, 49], was used for the discretization and the subsequent solution procedure. Essential BCs in Equation (53) were not encoded within the basis functions but enforced by additional Lagrange multipliers (i.e. η_α, γ and υ in Equation (61)). In such a mixed formulation, normal displacement gradient line BCs $(53)_2$ are enforced in terms of the auxiliary field M, while displacement line BCs $(53)_1$ are enforced in terms of the field u. Quadratic Lagrangian polynomials were used as basis functions for the fields χ and M. All Lagrange multiplier fields were discretized by linear Lagrange polynomials. The mesh was Delaunay tessellated with maximum diameter size equal to 8.45 mm (see Figure 3). Energy convergence of the solutions was successfully checked for the mesh-size tending to zero. The solution of each step, i.e. for each $\bar{u}$, was initialized by the solution of the previous one, considering for $\bar{u}$ a constant step-size $\Delta\bar{u}$ equal to 1 mm.

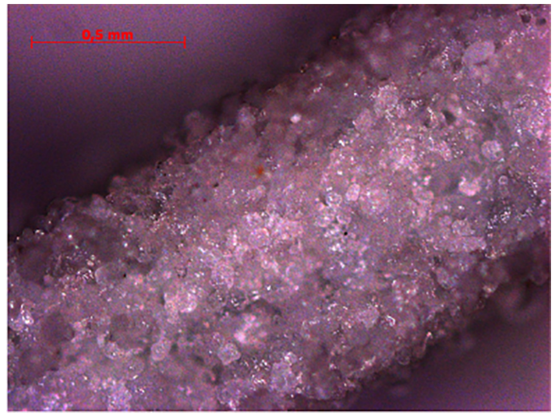

Figure 4. Micrograph of a monolithic slender element of the prototype showing granularity of printed polyamide.

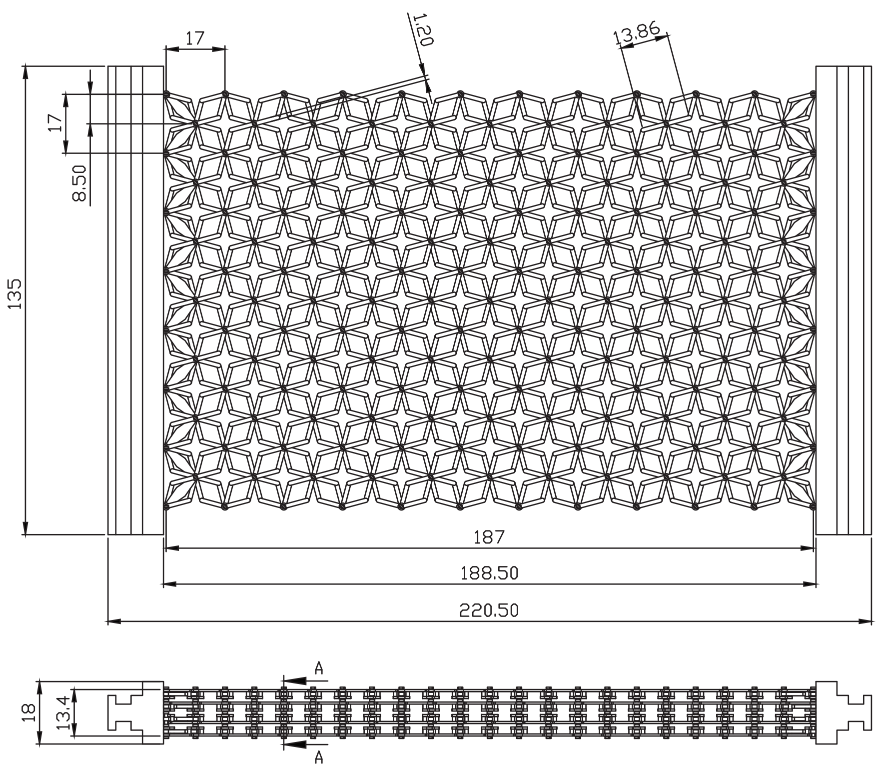

Figure 5. Technical drawing of the designed bi-pantographic prototypes. Top-view (top) and profile view (bottom). All lengths are expressed in millimetres.

4. Materials and methods

4.1. Manufacturing

Specimens were 3D printed using a selective laser sintering (SLS) procedure. Polyamide powder was used as raw material. Possible use of metallic powders is to be investigated [50-52]. A picture obtained by optical microscopy showing the granularity of the printed polyamide is presented in Figure 4. Modelling at lower scales taking into account such a granular structure [53-56] might be considered in future investigations.

All specimens were designed in SolidWorks computer-aided design (CAD) software by sketching 2D profiles and then using methods such as extruding and lofting in order to produce solid shapes, see the technical drawings in Figures 5, 6 and 10 (right). A full top-view of the manufactured specimen is shown

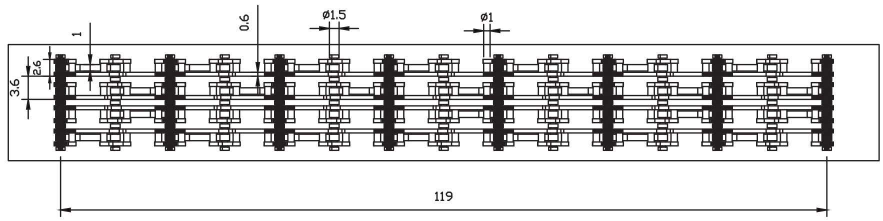

Figure 6. Section A–A indicated in Figure 5 (bottom). All lengths are expresses in millimetres.

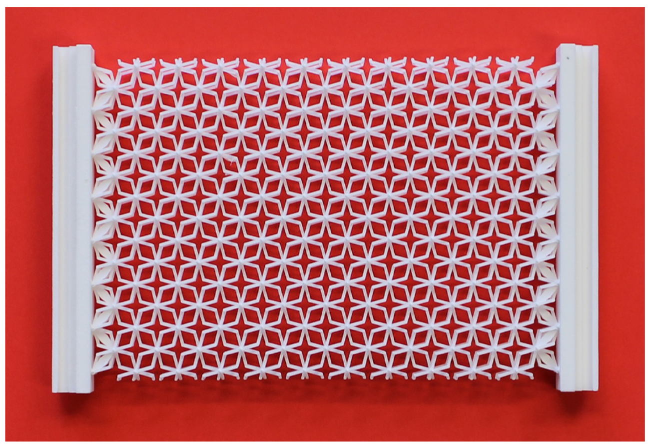

Figure 7. Full top-view of bi-pantographic prototype manufactured according to the technical drawings in Figures 5, 6 and 10 (right).

in Figure 7. The blue/red rotational springs in Figure 2(c) and the adjacent extensional ones are fabricated as a whole by means of monolithic slender elements that are meant to predominantly bend (rotational spring) and (to a lesser extent) extend (extensional springs) in plane. Such elements are combined at extreme points by cylinders, which are meant to reproduce the green rotational springs of Figure 2(c) by mainly twisting, and at middle points by hinge connections. They are shown in Figure 8 (actual manufacturing on the left (a) and CAD modelling on the right (b)). As assumed above, the angle γ is equal to $\pi/6$, see Figure 10 (right).

Each pantographic beam is made of two families of monolithic slender elements forming an angle 2γ and lying onto two different parallel planes. The two families of pantographic beams (whose centrelines form an angle of 90°) lying on two different planes are hinge connected at intersection points, which is at the mid-point of the monolithic slender elements. The structure is then doubled in the out-of-plane direction by reflection to avoid noticeable out-of-plane movements, making it symmetric with respect to its middle plane, see Figure 5 (bottom). Hinge axes are monolithic elements running through the full out-of-plane length of the structure.

Hard-device conditions given in rows three and six of Table 1 are obtained by connecting the adjacent hinge axes in proximity of the gripping areas, see Figure 9, with stocky rhomboidal elements, meant to be rigid with respect to other elements of the specimen for the considered load range.

4.2. Testing and data acquisition

An MTS Tytron 250 testing device was used for the experiments. The total reaction force was measured by a device own load cell, which is able to record axial forces in a range of ± 250 N with an accuracy of 0.2%. Increasing displacements were prescribed horizontally on the right side of the specimen with a loading rate of 15 mm/min. The cross-head displacement was measured and monitored by a device own encoder unit. Almost frictionless movement of the machine shaft was achieved by using an air-film bearing. External vibrations were avoided by placing the system on a massive concrete substructure. Pictures

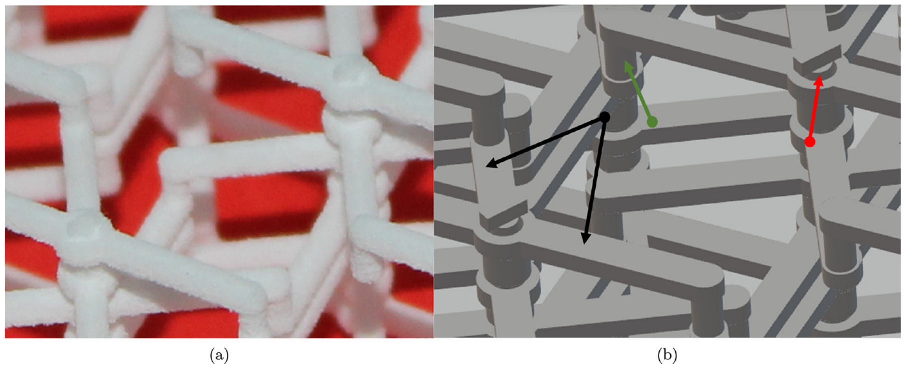

Figure 8. Manufactured specimen (a) and CAD design (b). Enlarged view of: 1. monolithic slender elements corresponding, by means of bending and extension, to blue/red rotational springs and to the adjacent extensional springs of Figure 2(c) (black arrows); 2. cylinders materializing, by means of torsion, the green rotational springs of Figure 2(c) (green arrow); and 3. hinges connecting monolithic slender elements at middle points (red arrow).

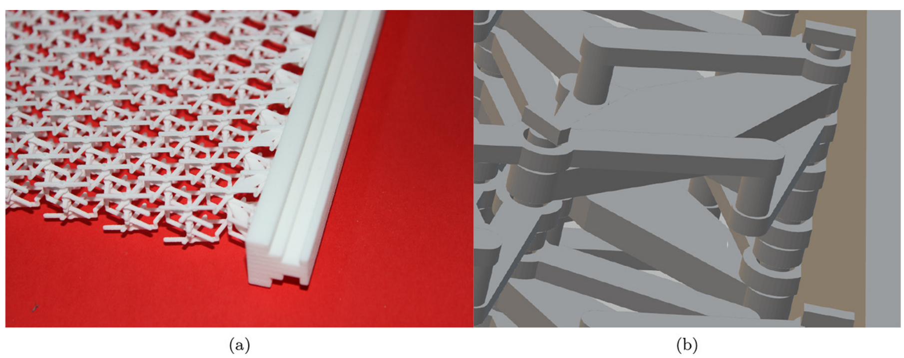

Figure 9. Realization of BCs listed in Table 1. Manufactured specimen (a) and enlarged view of its CAD design (b).

of the surface during deformations were taken (0.5 pictures/second) by means of a Canon EOS 600D camera with a definition of 4272×2848 pixels. Each picture was synchronized with the recorded force–displacement data in real time. Regarding frictional dissipation due to PA2200 powder stuck in hinges, four loading–unloading cycles were performed for maximum prescribed displacements equal to 10 mm, 20 mm, 30 mm, 40 mm, and 50 mm, respectively. No out-of-plane movements of the specimen was observed. For all cycles, residual (negative compression) total reaction force following unloading was less than 2% of the total reaction force peak. Figure 10(a) shows a picture of the deformed specimen.

4.3. DIC

The kinematic results described in the following were obtained via DIC. DIC consists of measuring displacement fields by registering pictures acquired during mechanical tests [57-59]. Various approaches have been introduced, namely, local (i.e. subset-based) analyses [60-62], and global (e.g. finite-element-based) techniques [63-65]. When dealing with pantographic structures, finite-element-based analyses have recently been performed at macroscopic [66] and mesoscopic scales [67]. In the present case, the sought kinematics corresponds to the in-plane displacements of the hinges at positions $p_{i,j}$ of the bi-pantographic structure. The analysis of the displacement of these discrete points is performed via local DIC, i.e. using zones of interest (ZOIs) [68] centred on each hinge. The simplest approach seeks the rigid body translation of each considered ZOI, as originally performed in particle image velocimetry [69-73]. Let f and g be the initial and current grey level images, respectively. For each ZOI, the correlation product

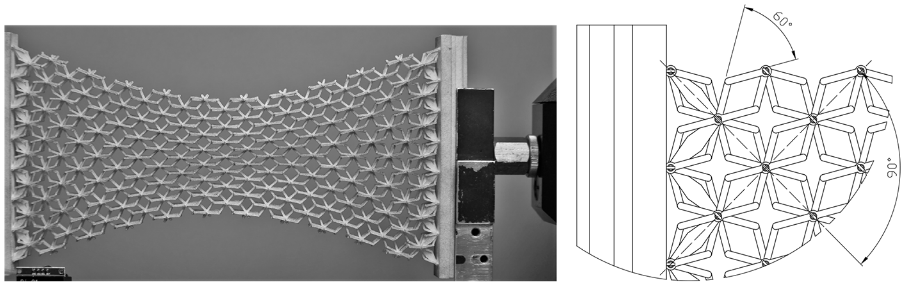

(a) (b)

Figure 10. Deformed specimen (a) and enlarged view (b) of the top-left corner of Figure 5 (top).

$$T(u) = \mathrm{Argmax}_v \sum_{\mathrm{ZOI}} f(x,y) g(x + \boldsymbol{v} \cdot e_x, y + \boldsymbol{v} \cdot e_y) \tag{64}$$

is maximized with respect to the rigid body translations $\boldsymbol{v} \in \mathbb{R}^2$. The computation of the correlation product can be performed in Fourier space (thanks to the shift/modulation property) via fast Fourier transforms (FFTs) to speed up the calculations [74]. No subpixel resolution [68] was sought in the present case because the expected displacements were very large when expressed in terms of pixels. Further, to account for the local angular variations between the beams connected by the hinges, the DIC calculations were performed incrementally, namely, for a series of pictures, the deformed picture of the nth registration step becomes the reference picture of the $n+1$th step, and the corresponding displacement increment is cumulated with the previous ones to provide a Lagrangian estimation of the hinge displacements. Last, for each analysis, two passes were performed. The first used a rather large ZOI size (i.e. 100×100 pixels) to obtain a robust first estimate. The second one utilized a smaller size (i.e. 50×50 pixels) to focus on the kinematic analysis about each hinge.

5. Results

The focus of this section is to present results obtained by the continuum model, and discuss how much they deviate from the experimental data. Owing to symmetry arguments (i.e. $D4$ [3] symmetry with respect to pantographic beam directions, symmetry of the specimen and BCs with respect to specimen's axes), it is concluded that the following symmetries should be fulfilled by the continuum solution (analogous statements can be done for the discrete one) with the notation $g(\zeta, \varsigma)$ standing for $g[x(\zeta, \varsigma), y(\zeta, \varsigma)]$

$$\begin{aligned} \vartheta_y(\zeta, \varsigma) &= \vartheta_x(\zeta, \ell - \varsigma), \quad \rho_y(\zeta, \varsigma) = \rho_x(L - \zeta, \varsigma) \\ \rho_y(\zeta, \varsigma) &= \rho_x(\zeta, \ell - \varsigma), \quad \vartheta_y(\zeta, \varsigma) = \vartheta_x(L - \zeta, \varsigma) \end{aligned} \tag{65}$$

and

$$\vartheta_y(\zeta, \varsigma) = \vartheta_y(L - \zeta, \ell - \varsigma), \quad \rho_y(\zeta, \varsigma) = \vartheta_y(L - \zeta, \ell - \varsigma) \tag{66}$$

As in the considered problem either $0 < \vartheta_x(x,y) < \pi/2$ and $-\pi/2 < \vartheta_y(x,y) < 0$ or $0 < \vartheta_y(x,y) < \pi/2$ and $-\pi/2 < \vartheta_x(x,y) < 0$, this can be seen a posteriori by looking at Figure 14), then the shear angle, which is null in the undeformed configuration and objective, is written in an easier way as $\pi/2 - |\vartheta_x| - |\vartheta_y|$. An analogous observation holds for the micro-model.

The maximum prescribed displacement $\bar{u}$ directed along ζ is equal to 50 mm. Parameters for the continuum (K_F, K_E and K_S) were found by fitting three curves (see Figure 11 and cf. also [11] where the same quantities, although defined for pantographic fabrics, were used for fitting). The first (Figure 11 (left)) is the total reaction force along the direction ζ (determined by the load cell of the testing machine) versus $\bar{u}$ (determined by the machine encoder unit). The second (Figure 11 (centre)) is the shear angle at point A (determined by DIC, see Figure 3) versus $\bar{u}$. Finally, the third (Figure 11 (right)) is the shear angle at

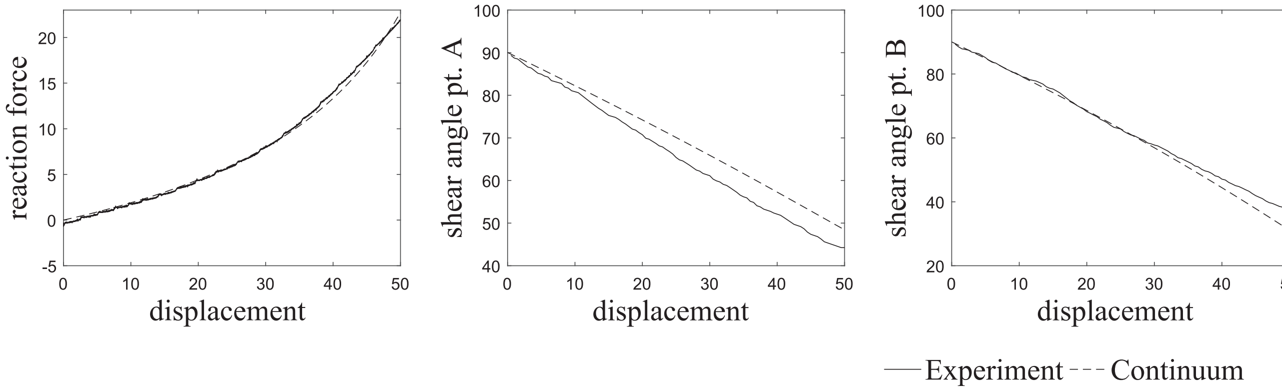

Figure 11. Total reaction force along the direction ζ with changed sign (N) versus prescribed displacement $\bar{u}$ (mm) along the direction e_ζ (left), shear angle at point A (°) versus prescribed displacement $\bar{u}$ (mm) along the direction e_ζ (centre), and shear angle (°) at point B versus prescribed displacement $\bar{u}$ (mm) along the direction e_ζ (right).

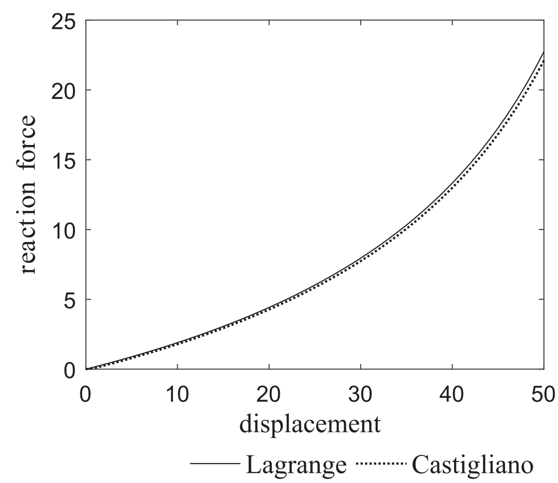

Figure 12. Total reaction force along the direction ζ with changed sign (N) versus $\bar{u}$ (mm) as computed by the continuum model using Lagrange multipliers and Castigliano's theorem. The forward finite difference approximation of $\partial\mathcal{E}/\partial\bar{u}$ has been computed with a step size for $\bar{u}$ equal to $\Delta\bar{u} = 1$ mm.

point B (determined by DIC, see Figure 3) versus $\bar{u}$. The total reaction force acting on Ω_3 has been found for the continuum model by means of Castigliano's theorem.

In order to check that computed Lagrange multipliers were consistent with the reaction force found by such a theorem, i.e. with energy conservation, one can compute the total reaction force acting on Ω_3 with the Lagrange multipliers as

$$-\int_{\Omega_3} \boldsymbol{\upsilon} \cdot \zeta \, \mathrm{d}l \tag{67}$$

This fact holds true for the numerical solution. Figure 12 compares the total reaction force along the direction ζ, as computed by the continuum model using Lagrange multipliers and Castigliano's theorem, versus $\bar{u}$. The forward finite difference approximation of $\partial\mathcal{E}/\partial\bar{u}$ was computed with a step size for $\bar{u}$ equal to $\Delta\bar{u} = 1$ mm. It is concluded that, up to finite difference discretization errors, the results obtained with the two methodologies are consistent. Owing to symmetry arguments, the total reaction force along the direction ς as computed with Lagrange multipliers should be cancelling out. In addition, this fact holds true for the numerical solution.

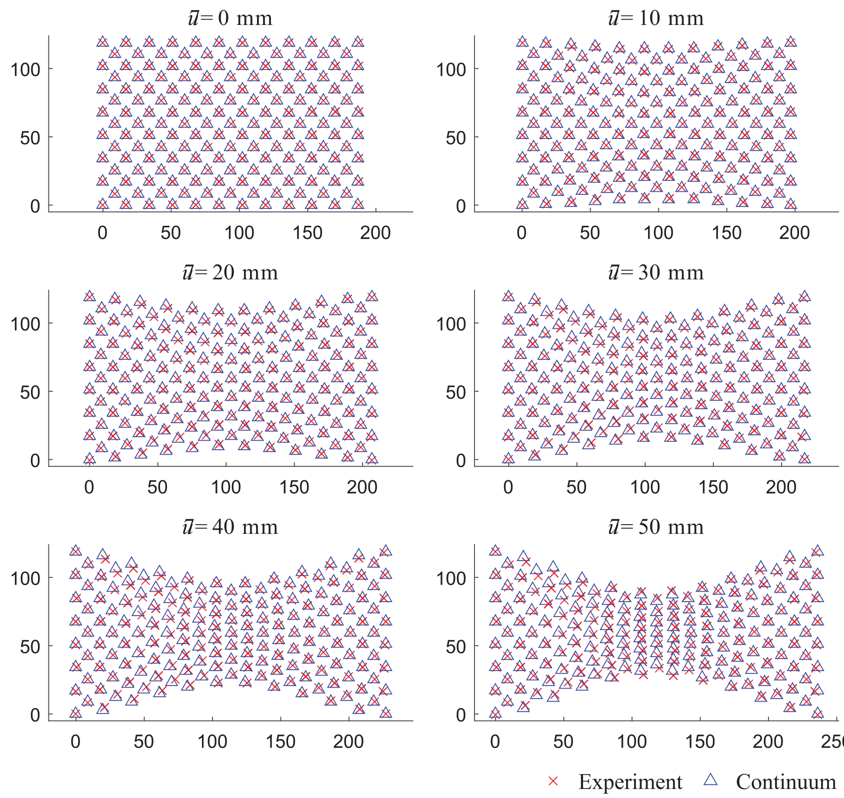

Figure 13. The deformed configuration as computed by the continuum model, i.e. $\chi(x_i, y_j)$, is compared for different applied $\bar{u}$ with experimental measurements. Abscissas and ordinates are expressed in millimeters.

The fitted values of the parameters for the continuum model are $K_F = 0.9$ J, $K_E = 0.33$ J, $K_S = 34$ N$\cdot$m^{-1}. Hence, the continuum model is capable of describing the considered experimental curves with only three constitutive parameters. The computed deformed configuration, i.e. $\chi(x_i, y_j)$, is compared for different prescribed $\bar{u}$ levels with experimentally measured data in Figure 13. It is seen that experimental measurements by DIC and the continuum model agree very well. Experimental data, unlike the continuum model, exhibit a non-symmetry which is especially evident for $\bar{u} = 40$ mm and $\bar{u} = 50$ mm on the left. It is worth noting that only the use of homogenization starting from a discrete model, with a target model not chosen a priori, allows such complex deformation energy to be recovered. The underlying family of discrete systems does not only lead to the deformation energy but also allows for a clear interpretation of non-standard BCs that appear in this formulation.

Contour plots of the y-stretch ρ_y are shown in Figure 14 for the continuum model.Figure 14 shows that the stretch is remarkably non-localized. This is due to pantographic beams being complete second gradient continua.

Let us quantify the sensitivity of the numerical simulation with respect to the application of non-standard zero normal displacement gradient BC $[\nabla u(x, y)]n(x, y) = 0$ on $\Omega_1 \cup \Omega_3$. In Figure 15, the quantities ρ_y and ϑ_y are plotted as functions of the local abscissa Φ of the boundary Ω_1 for the continuum model in both cases when zero normal displacement gradient BCs are enforced and when they are not ($\bar{u} = 50$ mm). In particular, in the vicinity of vertices of the domain Ω, the solution is strongly sensitive to the application of non-standard BCs.

6. Conclusion and outlook

Bi-pantographic fabrics proved to have an extremely wide elastic range. This is possible because in such structures the total deformation is much greater than single-elastic-element deformations. Compatibly

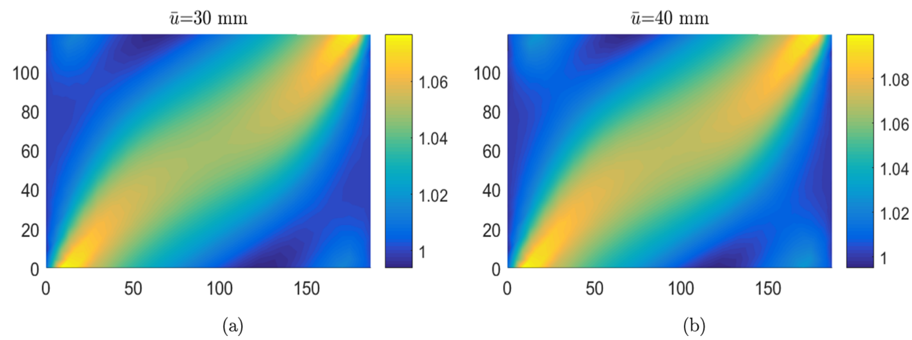

Figure 14. The y-stretch ρ_y as computed by the continuum model. Abscissas and ordinates are expressed in millimetres.

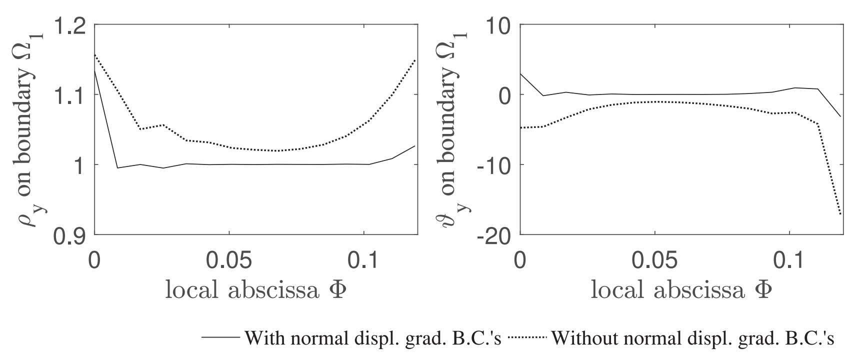

Figure 15. Plots of ρ_y (left) and of ϑ_y (°, right) versus the local abscissa Φ (m) of the boundary Ω_1 for continuum modelling when $\bar{u} = 50$ mm. The (arc-length) abscissa Φ is introduced in Figure 3.

with BCs and internal connection constraints, the elements arrange so as to minimize the total deformation energy by mimicking the wide variety of mechanisms corresponding to floppy modes.

Some future outlooks of the present work are:

- designing, experimenting and analysing a bi-pantographic system obeying the discrete model with $k_S = 0$, which would mean that all cylinders connecting slender monolithic elements would be replaced by hinges, giving a purely second gradient material at the macro-scale;
- studying the dynamics of bi-pantographic fabrics, which could be done by exploiting the results already obtained for pantographic beams [75];
- studying out-of-plane deformations [76] of such metamaterials.

Acknowledgements

The authors thank P. Seppecher, G. Ganzosch and T. Lekszycki for stimulating discussions.

Funding

The author(s) received no financial support for the research, authorship, and/or publication of this article.

Notes

1 Here D denotes *dextrum* and S denotes *sinistrum*.

ORCID iD

Emilio Barchiesi https://orcid.org/0000-0002-7296-0671

References

[1] Harrison, P. Modelling the forming mechanics of engineering fabrics using a mutually constrained pantographic beam and membrane mesh. *Composites A: Appl Sci Manuf* 2016; 81: 145–157.
[2] Andreaus, U, dell'Isola, F, Giorgio, I, et al. Numerical simulations of classical problems in two-dimensional (non) linear second gradient elasticity. *Int J Eng Sci* 2016; 108: 34–50.
[3] Auffray, N, Dirrenberger, J, and Rosi, G. A complete description of bi-dimensional anisotropic strain-gradient elasticity. *Int J Solids Structures* 2015; 69: 195–206.
[4] Battista, A, Rosa, L, dell'Erba, R, et al. Numerical investigation of a particle system compared with first and second gradient continua: Deformation and fracture phenomena. *Math Mech Solids* 2017; 22(11): 2120–2134.
[5] Steigmann, DJ. The variational structure of a nonlinear theory for spatial lattices. *Meccanica* 1996; 31(4): 441–455.
[6] Turco, E, dell'Isola, F, Rizzi, N, et al. Fiber rupture in sheared planar pantographic sheets: Numerical and experimental evidence. *Mech Res Commun* 2016; 76: 86–90.
[7] Turco, E, Golaszewski, M, Cazzani, A, et al. Large deformations induced in planar pantographic sheets by loads applied on fibers: Experimental validation of a discrete Lagrangian model. *Mech Res Commun* 2016; 76: 51–56.
[8] Turco, E, Barcz, K, Pawlikowski, M, et al. Non-standard coupled extensional and bending bias tests for planar pantographic lattices. Part I: Numerical simulations. *Z angew Math Phys* 2016; 67(5): 122.
[9] Turco, E, Giorgio, I, Misra, A, et al. King post truss as a motif for internal structure of (meta) material with controlled elastic properties. *R Soc Open Sci* 2017; 4(10).
[10] Turco, E, dell'Isola, F, Cazzani, A, et al. Hencky-type discrete model for pantographic structures: Numerical comparison with second gradient continuum models. *Z angew Math Phys* 2016; 67: 85.
[11] dell'Isola, F, Giorgio, I, Pawlikowski, M, et al. Large deformations of planar extensible beams and pantographic lattices: heuristic homogenization, experimental and numerical examples of equilibrium. *Proc R Soc A* 2016; 472: 2185.
[12] Babuška, I. Homogenization approach in engineering. In *Computing methods in applied sciences and engineering*. Berlin: Springer, 1976, pp. 137–153.
[13] Allaire, G. Homogenization and two-scale convergence. *SIAM J Math Anal* 1992; 23(6): 1482–1518.
[14] Tartar, L. *The General Theory of Homogenization: A Personalized Introduction*, Vol. 7. Springer Science & Business Media, 2009.
[15] Yu, W, and Tang, T. Variational asymptotic method for unit cell homogenization. In *Advances in Mathematical Modeling and Experimental Methods for Materials and Structures*. Berlin: Springer, 2009, pp. 117–130.
[16] dell'Isola, F, Maier, G, Perego, U, et al. *The Complete Works of Gabrio Piola*, Vol. I. Cham, Switzerland: Springer, 2014.
[17] Golaszewski, M, Grygoruk, R, Giorgio, I, et al. Metamaterials with relative displacements in their microstructure: Technological challenges in 3D printing, experiments and numerical predictions. *Continuum Mech Thermodyn* 2018; 31(4): 1015–1034.
[18] Milton, G, Briane, M, and Harutyunyan, D. On the possible effective elasticity tensors of 2-dimensional and 3-dimensional printed materials. *Math Mech Complex Syst* 2017; 5(1): 41–94.
[19] Milton, G, Harutyunyan, D, and Briane, M. Towards a complete characterization of the effective elasticity tensors of mixtures of an elastic phase and an almost rigid phase. *Math Mech Complex Syst* 2017; 5(1): 95–113.
[20] Abdoul-Anziz, H, and Seppecher, P. Strain gradient and generalized continua obtained by homogenizing frame lattices. *Math Mech Complex Syst* 2018; 6(3): 213–250.
[21] Barchiesi, E, Spagnuolo, M, and Placidi, L. Mechanical metamaterials: A state of the art. *Math Mech Solids* 2019; 24(1): 212–234.
[22] Di Cosmo, F, Laudato, M, and Spagnuolo, M. Acoustic metamaterials based on local resonances: Homogenization, optimization and applications. In *Generalized Models and Non-classical Approaches in Complex Materials 1*. Berlin: Springer, 2018, pp. 247–274.
[23] dell'Isola, F, Lekszycki, T, Pawlikowski, M, et al. Designing a light fabric metamaterial being highly macroscopically tough under directional extension: First experimental evidence. *Z angew Math Phys* 2015; 66: 3473–3498.
[24] Giorgio, I, Della Corte, A, dell'Isola, F, et al. Buckling modes in pantographic lattices. *C R Mecanique* 2016; 344(7): 487–501.
[25] Giorgio, I, Della Corte, A, and dell'Isola, F. Dynamics of 1D nonlinear pantographic continua. *Nonlinear Dynamics* 2017; 88(1): 21–31.
[26] Placidi, L, Barchiesi, E, Turco, E, et al. A review on 2D models for the description of pantographic fabrics. *Z angew Math Phys* 2016; 67(5): 121.
[27] Placidi, L, Andreaus, U, and Giorgio, I. Identification of two-dimensional pantographic structure via a linear d4 orthotropic second gradient elastic model. *J Eng Math* 2017; 103(1) 1–21.
[28] Giorgio, I. Numerical identification procedure between a micro-cauchy model and a macro-second gradient model for planar pantographic structures. *Z angew Math Phys* 2016; 67(4): 95.
[29] Cuomo, M, dell'Isola, F, and Greco, L. Simplified analysis of a generalized bias test for fabrics with two families of inextensible fibres. *Z angew Math Phys* 2016; 67(3): 61.

[30] Turco, E, Misra, A, Pawlikowski, M, et al. Enhanced Piola–Hencky discrete models for pantographic sheets with pivots without deformation energy: Numerics and experiments. *Int J Solids Structures* 2018; 147: 94–109.
[31] Misra, A, Lekszycki, T, Giorgio, I, et al. Pantographic metamaterials show atypical poynting effect reversal. *Mech Res Commun* 2018; 89: 6–10.
[32] Eremeyev, VA, dell'Isola, F, Boutin, C, et al. Linear pantographic sheets: existence and uniqueness of weak solutions. *J Elasticity* 2018; 132(2): 175–196.
[33] Barchiesi, E, dell'Isola, F, Laudato, M, et al. A 1D continuum model for beams with pantographic microstructure: Asymptotic micro–macro identification and numerical results. In: *Advances in Mechanics of Microstructured Media and Structures*. Berlin: Springer, 2018, pp. 43–74.
[34] Alibert, JJ, Seppecher, P, and dell'Isola, F. Truss modular beams with deformation energy depending on higher displacement gradients. *Math Mech Solids* 2003; 8(1): 51–73.
[35] Seppecher, P, Alibert, JJ, and dell'Isola, F. Linear elastic trusses leading to continua with exotic mechanical interactions. In *J Phys Conf Ser* 319: 012018.
[36] Barchiesi, E, Eugster, SR, Placidi, L, et al. Pantographic beam: A complete second gradient 1D-continuum in plane. *Z angew Math Phys* 2019; 70(5): 135.
[37] dell'Isola, F, Seppecher, P, and Della Corte, A. The postulations á la d'Alembert and á la Cauchy for higher gradient continuum theories are equivalent: A review of existing results. *Proc R Soc A* 471: 2183.
[38] dell'Isola, F, Madeo, A, and Seppecher, P. Cauchy tetrahedron argument applied to higher contact interactions. *Arch Rat Mech Anal* 2016; 219(3): 1305–1341.
[39] dell'Isola, F, and Steigmann, D. A two-dimensional gradient-elasticity theory for woven fabrics. *J Elasticity* 2015; 18: 113–125.
[40] Eugster, SR, and Glocker, C. On the notion of stress in classical continuum mechanics. *Math Mech Complex Syst* 2017; 5(3–4): 299–338.
[41] Steigmann, D, and Faulkner, M. Variational theory for spatial rods. *J Elasticity* 1993; 33(1): 1–26.
[42] Germain, P. The method of virtual power in continuum mechanics. Part 2: Microstructure. *SIAM J Appl Math* 1973; 25: 556–575.
[43] Forest, S, and Sievert, R. Nonlinear microstrain theories. *Int J Solids Structures* 2006; 43(24): 7224–7245.
[44] Eremeyev, VA, Lebedev, LP, and Altenbach, H. *Foundations of Micropolar Mechanics*. Springer Science & Business Media, 2012.
[45] Altenbach, H, Brsan, M, and Eremeyev, VA. Cosserat-type rods. In: *Generalized Continua from the Theory to Engineering Applications*. Berlin: Springer, 2013, pp. 179–248.
[46] Auffray, N, dell'Isola, F, Eremeyev, V, et al. Analytical continuum mechanics à la Hamilton–Piola least action principle for second gradient continua and capillary fluids. *Math Mech Solids* 2015; 20(4): 375–417.
[47] Bersani, A, dell'Isola, F, and Seppecher, P. Lagrange multipliers in infinite dimensional spaces, examples of application. In: Altenbach, H, and Öchsner, A (eds.) *Encyclopedia of Continuum Mechanics*. Berlin: Springer.
[48] Abali, B, Müller, W, and Eremeyev, V. Strain gradient elasticity with geometric nonlinearities and its computational evaluation. *Mech Adv Mater Modern Processes* 2015; 1(1): 4.
[49] Abali, BE, Müller, WH, and dell'Isola, F. Theory and computation of higher gradient elasticity theories based on action principles. *Arch Appl Mech* 2017; 87(9): 1495–1510.
[50] Spagnuolo, M, Barcz, K, Pfaff, A, et al. Qualitative pivot damage analysis in aluminum printed pantographic sheets: numerics and experiments. *Mech Res Commun* 2017; 83: 47–52.
[51] Spagnuolo, M, Peyre, P, and Dupuy, C. Phenomenological aspects of quasi-perfect pivots in metallic pantographic structures. *Mech Res Commun* 2019; 101: 103415.
[52] De Angelo, M, Spagnuolo, M, D'Annibale, F, et al. The macroscopic behavior of pantographic sheets depends mainly on their microstructure: Experimental evidence and qualitative analysis of damage in metallic specimens. *Continuum Mech Thermodyn* 2019; 31(4): 1181–1203.
[53] Misra, A, and Singh, V. Micromechanical model for viscoelastic materials undergoing damage. *Continuum Mech Thermodyn* 2013; 25(2–4): 343–358.
[54] Misra, A, and Poorsolhjouy, P. Granular micromechanics model for damage and plasticity of cementitious materials based upon thermomechanics. *Math Mech Solids* 2015. DOI: 10.1177/1081286515576821.
[55] Misra, A, and Singh, V. Thermomechanics-based nonlinear rate-dependent coupled damage-plasticity granular micromechanics model. *Continuum Mech Thermodyn* 2015; 27(4–5): 787.
[56] Misra, A, and Ching, W. Theoretical nonlinear response of complex single crystal under multi-axial tensile loading. *Sci Rep* 2013; 3: 1488.
[57] Sutton, M, McNeill, S, Helm, J, et al. *Advances in Two-Dimensional and Three-Dimensional Computer Vision (Topics in Applied Physics,* Vol. 77). Berlin: Springer, 2000, pp. 323–372.
[58] Sutton, M, Orteu, J, and Schreier, H. *Image Correlation for Shape, Motion and Deformation Measurements: Basic Concepts, Theory and Applications*. New York: Springer, 2009.

[59] Sutton, M. Computer vision-based, noncontacting deformation measurements in mechanics: A generational transformation. *Appl Mech Rev* 2013; 65: 050802.
[60] Peters, W, and Ranson, W. Digital imaging techniques in experimental stress analysis. *Opt Eng* 1982; 21: 427–431.
[61] Sutton, M, Wolters, W, Peters, W, et al. Determination of displacements using an improved digital correlation method. *Im Vis Comp* 1983; 1(3): 133–139.
[62] Chu, T, Ranson, W, Sutton, M, et al. Applications of digital-image-correlation techniques to experimental mechanics. *Exp Mech* 1985; 3(25): 232–244.
[63] Broggiato, G. Adaptive image correlation technique for full-field strain measurement. In Pappalettere, C (ed.) *12th Int. Conf. Exp. Mech.* McGraw Hill, Lilan (Italy), pp. 420–421.
[64] Sun, Y, Pang, J, Wong, C, et al. Finite-element formulation for a digital image correlation method. *Appl Optics* 2005; 44(34): 7357–7363.
[65] Besnard, G, Hild, F, and Roux, S. "Finite-element" displacement fields analysis from digital images: Application to Portevin–Le Chatelier bands. *Exp Mech* 2006; 46: 789–803.
[66] Turco, E, Misra, A, Pawlikowski, M, et al. Enhanced Piola-Hencky discrete models for pantographic sheets with pivots without deformation energy: Numerics and experiments. *Int J Solids Structures* 2018; 147: 94–109.
[67] dell'Isola, F, Seppecher, P, Alibert, JJ, et al. Pantographic metamaterials: An example of mathematically-driven design and of its technological challenges. *Continuum Mech Thermodyn* 2019. DOI: 10.1007/s00161-018-0689-8.
[68] Hild, F, Raka, B, Baudequin, M, et al. Multi-scale displacement field measurements of compressed mineral wool samples by digital image correlation. *Appl Optics* 2002; IP 41(32): 6815–6828.
[69] Barker, D, and Fourney, M. Measuring fluid velocities with speckle patterns. *Optics Lett* 1977; 1: 135–137.
[70] Dudderar, T, and Simpkins, P. Laser speckle photography in a fluid medium. *Nature* 1977; 270: 45–47.
[71] Grousson, R, and Mallick, S. Study of flow pattern in a fluid by scattered laser light. *Appl Optics* 1977; 16: 2334–2336.
[72] Adrian, R. Scattering particle characteristics and their effect on pulsed laser measurements of fluid flow: Speckle velocimetry vs. particle image velocimetry. *Appl Optics* 1984; 23: 1690–1691.
[73] Adrian, R. Twenty years of particle image velocimetry. *Exp Fluids* 2005; 39: 159–169.
[74] Hild, F, and Roux, S. Digital image correlation. In: Rastogi, P, and Hack, E (eds.) *Optical Methods for Solid Mechanics. A Full-Field Approach*. Weinheim: Wiley-VCH, 2012, pp. 183–228.
[75] Barchiesi, E, Laudato, M, and Di Cosmo, F. Wave dispersion in non-linear pantographic beams. *Mech Res Commun* 2018; 94: 128–132.
[76] Giorgio, I, Rizzi, N, and Turco, E. Continuum modelling of pantographic sheets for out-of-plane bifurcation and vibrational analysis. *Proc R Soc A: Math Phys Eng Sci* 2017; 473(2207): 20170636.

Appendix A

The terms θ_i and $\varphi_i^{\mu S} - \varphi_i^{\mu D}$ are expanded up to first order by using the definitions (1) and (3) together with the expansions (13) and (14). According to (12) and (13) the vectors between two adjacent points p_i are

$$p_{i+1} - p_i = \varepsilon\left[\chi'(s_i) + \frac{\varepsilon}{2}\chi''(s_i) + o(\varepsilon)\right], \quad p_i - p_{i-1} = \varepsilon\left[\chi'(s_i) - \frac{\varepsilon}{2}\chi''(s_i) + o(\varepsilon)\right]. \tag{68}$$

The arguments of $\tan^{-1}$ in (3) are written as functions of ε

$$\begin{aligned} h_{i+1}(\varepsilon) &= \frac{(p_{i+1} - p_i)\cdot e_y}{(p_{i+1} - p_i)\cdot e_x} \overset{(68)_1}{=} \frac{\chi'(s_i)\cdot e_y + \frac{\varepsilon}{2}\chi''(s_i)\cdot e_y + o(\varepsilon)}{\chi'(s_i)\cdot e_x + \frac{\varepsilon}{2}\chi''(s_i)\cdot e_x + o(\varepsilon)}, \\ h_i(\varepsilon) &= \frac{(p_i - p_{i-1})\cdot e_y}{(p_i - p_{i-1})\cdot e_x} \overset{(68)_2}{=} \frac{\chi'(s_i)\cdot e_y - \frac{\varepsilon}{2}\chi''(s_i)\cdot e_y + o(\varepsilon)}{\chi'(s_i)\cdot e_x - \frac{\varepsilon}{2}\chi''(s_i)\cdot e_x + o(\varepsilon)}. \end{aligned} \tag{69}$$

It is noted that $h_i(0) = h_{i+1}(0) = \left[\chi'(s_i)\cdot e_y\right]/\left[\chi'(s_i)\cdot e_x\right]$. Moreover,

$$\begin{aligned} {h_{i+1}}'(0) = -h'_i(0) &= \frac{1}{2[\chi'\cdot e_x]^2}\left[(\chi''\cdot e_y)(\chi'\cdot e_x) - (\chi''\cdot e_x)(\chi'\cdot e_y)\right]\Big|_{s=s_i} \\ &= \frac{1}{2[\chi'\cdot e_x]^2}\chi''\cdot(e_y\otimes e_x - e_x\otimes e_y)\cdot\chi'\Big|_{s=s_i} = \frac{\chi''(s_i)\cdot{\chi'}_\perp(s_i)}{2[\chi'(s_i)\cdot e_x]^2}. \end{aligned} \tag{70}$$

For a real-valued function $h(\varepsilon)$, $\tan^{-1}(h(\varepsilon)) = \tan^{-1}(h(0)) + \frac{h'(0)}{1+h(0)^2}\varepsilon + o(\varepsilon)$. As $h_i(0) = h_{i+1}(0)$, the first terms in the Taylor series of both $\tan^{-1}$ expressions in (3) coincide

$$\begin{aligned}\theta_i = & \left[\frac{1}{1+h_{i+1}(0)^2}h_{i+1}{}'(0) - \frac{1}{1+h_i(0)^2}h_i{}'(0)\right]\varepsilon + o(\varepsilon)\\ & \overset{(70)}{=} \frac{1}{1+\left[\frac{\chi'(s_i)\cdot e_y}{\chi'(s_i)\cdot e_x}\right]^2}\frac{\chi''(s_i)\cdot\chi'_\perp(s_i)}{[\chi'(s_i)\cdot e_x]^2}\varepsilon + o(\varepsilon)\\ & = \frac{\chi''(s_i)\cdot\chi'_\perp(s_i)}{\|\chi'(s_i)\|^2}\varepsilon + o(\varepsilon) \overset{(11)}{=} \vartheta'(s_i)\varepsilon + o(\varepsilon).\end{aligned} \tag{71}$$

For the expansion (1), it is required to perform the expansion of the norm of a vector-valued function $a(\varepsilon)$, i.e. $\| a(\varepsilon) \| = \| a(0) \| + \frac{a(0)\cdot a'(0)}{\|a(0)\|}\varepsilon + o(\varepsilon)$. Taking $a(\varepsilon)$ to be the expansions appearing in the squared brackets of (68) and considering that $\rho(s) = \| \chi'(s) \|$,

$$\| p_{i\pm1} - p_i \| = \varepsilon\left[\| \chi'(s_i) \| \pm \frac{\chi'(s_i)\cdot\chi''(s_i)}{\| \chi'(s_i) \|}\frac{\varepsilon}{2} + o(\varepsilon)\right] = \varepsilon\left[\rho(s_i) \pm \rho'(s_i)\frac{\varepsilon}{2} + o(\varepsilon)\right]. \tag{72}$$

Consequently, the expansion of the squared expression of (72) reads

$$\| p_{i\pm1} - p_i \|^2 = \varepsilon^2\left[\| \chi' \|^2 \pm (\chi'\cdot\chi'')\varepsilon + o(\varepsilon)\right]_{s=s_i} = \varepsilon^2\left[\rho^2 \pm \rho\rho'\varepsilon + o(\varepsilon)\right]_{s=s_i}. \tag{73}$$

Using (14), (72) and (73) in the argument of $\cos^{-1}$ of $(1)_{1,2}$,

$$\begin{aligned} h^{1D(S)}(\varepsilon) &= \left.\frac{\varepsilon^2\left[\rho^2 - \rho\rho'\varepsilon + \varepsilon(1/\cos\gamma)(\tilde{l}^{1D(S)} - \tilde{l}^{2S(D)}) + o(\varepsilon)\right]}{2\varepsilon^2\left[1/2\cos\gamma + \tilde{l}^{1D(S)}\varepsilon + o(\varepsilon)\right][\rho - \rho'\varepsilon/2 + o(\varepsilon)]}\right|_{s=s_i}\\ &= \left.\frac{\rho^2 + \varepsilon\left[(1/\cos\gamma)(\tilde{l}^{1D(S)} - \tilde{l}^{2S(D)}) - \rho\rho'\right] + o(\varepsilon)}{(1/\cos\gamma)\rho + \varepsilon\left[2\tilde{l}^{1D(S)}\rho - (1/2\cos\gamma)\rho'\right] + o(\varepsilon)}\right|_{s=s_i}.\end{aligned} \tag{74}$$

Similarly, the expansions of the arguments of $\cos^{-1}$ appearing in $(1)_{3,4}$ read

$$h^{2S(D)}(\varepsilon) = \left.\frac{\rho^2 + \varepsilon\left[(1/\cos\gamma)(\tilde{l}^{2S(D)} - \tilde{l}^{1D(S)}) - \rho\rho'\right] + o(\varepsilon)}{(1/\cos\gamma)\rho + \varepsilon\left[2\tilde{l}^{2S(D)}\rho - (1/2\cos\gamma)\rho'\right] + o(\varepsilon)}\right|_{s=s_i}. \tag{75}$$

All functions are of the form $h^{\mu\nu}(\varepsilon) = [a + \varepsilon b^{\mu\nu} + o(\varepsilon)]/[c + \varepsilon d^{\mu\nu} + o(\varepsilon)]$ with $h^{\mu\nu}(0) = a/c$ and $(h^{\mu\nu})'(0) = (b^{\mu\nu}c - d^{\mu\nu}a)/c^2$. The angles $\varphi_i^{\mu\nu}$ are, thus, expanded as

$$\varphi_i^{\mu\nu} = \cos^{-1}[h^{\mu\nu}(0)] - \frac{\varepsilon}{\sqrt{1 - h^{\mu\nu}(0)^2}}(h^{\mu\nu})'(0) + o(\varepsilon). \tag{76}$$

Expanding $\varphi_i^{\mu S} - \varphi_i^{\mu D}$ with the help of (76), the first term thereof cancels. Inserting the derivative with respect to ε evaluated at $\varepsilon = 0$ of (74) and $(75)_1$,

$$\varphi_i^{1S} - \varphi_i^{1D} = \left.\frac{\rho^2(\tilde{l}^{1S} - \tilde{l}^{1D}) + (1/2\cos\gamma)\rho\rho' - (1/2\cos^2\gamma)(\tilde{l}^{1S} - \tilde{l}^{1D} + \tilde{l}^{2S} - \tilde{l}^{2D})}{\rho(1/2\cos\gamma)\sqrt{2}\sqrt{\frac{(1/\cos^2\gamma)-\rho^2}{2}}}\right|_{s=s_i} \varepsilon + o(\varepsilon)$$
$$= \left.\frac{\rho[\rho^2 - (1/2\cos^2\gamma)](\tilde{l}^{1S} - \tilde{l}^{1D}) + (1/2\cos\gamma)\rho^2\rho' + \rho(1/2\cos^2\gamma)(\tilde{l}^{2D} - \tilde{l}^{2S})}{\rho^2(1/2\cos\gamma)\sqrt{2}\sqrt{\frac{(1/\cos^2\gamma)-\rho^2}{2}}}\right|_{s=s_i} \varepsilon + o(\varepsilon). \tag{77}$$

In the same manner the expansion for the difference in angles of the oblique springs indexed by $\mu = 2$ is obtained. Moreover, the previous expressions are simplified to give

$$\varphi_i^{1(2)S} - \varphi_i^{1(2)D} = \left.\frac{4[\rho^2 - (1/2\cos^2\gamma)](\tilde{l}^{1(2)S} - \tilde{l}^{1(2)D}) + (1/\cos\gamma)(\rho^2)' + (2/\cos^2\gamma)(\tilde{l}^{2(1)D} - \tilde{l}^{2(1)S})}{4\rho(1/2\cos\gamma)\sqrt{(1/\cos^2\gamma) - \rho^2}}\right|_{s=s_i} \varepsilon + o(\varepsilon), \tag{78}$$

which, for $\gamma = \pi/6$, becomes

$$\varphi_i^{1(2)S} - \varphi_i^{1(2)D} = \left.\frac{\sqrt{3}(\rho^2 - 2/3)(\tilde{l}^{1(2)S} - \tilde{l}^{1(2)D}) + \rho\rho' + 2/\sqrt{3}(\tilde{l}^{2(1)D} - \tilde{l}^{2(1)S})}{\rho\sqrt{4/3 - \rho^2}}\right|_{s=s_i} \varepsilon + o(\varepsilon). \tag{79}$$

Using (14), (72) and (73) in the argument of $\cos^{-1}$ of (2), we can compute

$$h^{1(2)}(\varepsilon) = \frac{(l_i^{1(2)D})^2 + (l_{i+1}^{2(1)S})^2 - \| p_{i+1} - p_i\|^2}{2 l_i^{1(2)D} l_{i+1}^{2(1)S}}$$
$$= \left.\frac{\varepsilon^2\left[1/2\cos^2\gamma - \rho^2 + \rho\rho'\varepsilon + \varepsilon(1/\cos\gamma)(\tilde{l}^{1(2)D} + \tilde{l}^{2(1)S}) + o(\varepsilon)\right]}{2\varepsilon^2\left[1/2\cos\gamma + \tilde{l}^{1(2)D}\varepsilon + o(\varepsilon)\right][1/2\cos\gamma + \tilde{l}^{2(1)S}\varepsilon + o(\varepsilon)]}\right|_{s=s_i} \tag{80}$$
$$= \left.\frac{1/2\cos^2\gamma - \rho^2 + \varepsilon\left[\rho\rho' + (1/\cos\gamma)(\tilde{l}^{1(2)D} + \tilde{l}^{2(1)S})\right] + o(\varepsilon)}{1/2\cos^2\gamma + \varepsilon(1/\cos\gamma)(\tilde{l}^{1(2)D} + \tilde{l}^{2(1)S}) + o(\varepsilon)}\right|_{s=s_i}.$$

The angles ξ^1 and ξ^2 are, thus, expanded as

$$\xi_i^\mu = \cos^{-1}[h^\mu(0)] + o(\varepsilon^0) = \cos^{-1}\left(1 - \frac{\rho^2}{1/2\cos^2\gamma}\right)\bigg|_{s=s_i} + o(\varepsilon^0). \tag{81}$$

Thus, for $\gamma = \frac{\pi}{6}$,

$$\xi_i^\mu = \cos^{-1}\left(1 - \frac{3}{2}\rho^2\right)\bigg|_{s=s_i} + o(\varepsilon^0). \tag{82}$$

For the expansion of

$$K_S\left[\cos^{-1}\left(1 - \frac{\rho_\alpha^2}{1/2\cos^2\gamma}\right) - \pi + 2\gamma\right]^2 \tag{83}$$

in (47) with respect to ∇u required to obtain Equation (52), Equation (50) is inserted into the following

$$a\{\cos^{-1}\left[1-\frac{(x+1)^2}{1/2\cos^2 b}\right]+2b-\pi\}^2=[4a\cot b]x^2+o(x^2) \tag{84}$$

with $a, b \in \mathbb{R}$ to obtain

$$K_S\left[\cos^{-1}\left(1-\frac{\rho_\alpha^2}{1/2\cos^2\gamma}\right)-\pi+2\gamma\right]^2=[4K_S\cot\gamma]\left(\frac{\partial u}{\partial \alpha}\cdot e_\alpha\right)^2+o\left(\|\frac{\partial u}{\partial \alpha}\|^2\right). \tag{85}$$